Journal of the American College of Cardiology
© 2008 by the American College of Cardiology Foundation
Published by Elsevier Inc.

Vol. 51, No. 6, 2008
ISSN 0735-1097/08/$34.00
doi:10.1016/j.jacc.2007.10.030

# Localized Elevation of Shear Stress Is Related to Coronary Plaque Rupture

## A 3-Dimensional Intravascular Ultrasound Study With In-Vivo Color Mapping of Shear Stress Distribution

Yusaku Fukumoto, MD, Takafumi Hiro, MD, PHD, FACC, Takashi Fujii, MD, PHD, Genta Hashimoto, MD, Tatsuhiro Fujimura, MD, Jutaro Yamada, MD, PHD, Takayuki Okamura, MD, PHD, Masunori Matsuzaki, MD, PHD, FACC

*Yamaguchi, Japan*

**Objectives** The purpose of the present study was to assess the relationship between shear stress distribution and coronary plaque rupture by means of a new color-mapping program of shear stress with 3-dimensional intravascular ultrasound (IVUS).

**Background** Various in-vitro studies have demonstrated that shear stress of the vascular lumen is one of the important determinants of coronary plaque vulnerability. However, the in-vivo relationship between shear stress and plaque rupture is still unclear.

**Methods** In the present study, 3-dimensional IVUS was used to obtain spatial information on luminal geometry from 20 patients with acute coronary syndrome having a distinct ulcerative lesion. These 3-dimensional contours for each lumen were first reconstructed into mesh polygons, and then analyzed by means of a program for calculating the fluid dynamics. The flow was considered to be a constant laminar one. Then, colorized mappings of the distribution of the streamline, blood pressure, and shear stress were performed. The original luminal contour for each ruptured lesion was obtained by smoothing and extrapolation.

**Results** All patients had a coronary plaque rupture in the proximal or top portion of the plaque hill. In the color mapping, localized elevation of blood pressure and shear stress could be observed on each plaque surface. The shear stress concentration was frequently correlated with the plaque rupture site (kappa = 0.79).

**Conclusions** Although the absolute value of shear stress is not sufficient to directly provoke mechanical destruction of the fibrous cap, localized high shear stress might be a trigger of fibrous cap rupture. (J Am Coll Cardiol 2008;51: 645–50) © 2008 by the American College of Cardiology Foundation

Coronary plaque rupture with subsequent thrombus formation is the most important mechanism leading to acute coronary syndrome (ACS) (1–3). A plaque that is prone to rupture is denoted as vulnerable plaque. Such a plaque cluster is usually associated with eccentric noncalcified morphology (3,4), a thin fibrous cap (3,5–7), a large lipid core (3,5,6,8,9), infiltration of inflammatory cells (7,10), and spotty calcification (11). Coronary plaque rupture occurs frequently at the shoulder of eccentric plaques (8). It has been theoretically suggested that this portion is subjected to excessive concentration of circumferential tensile stress, which might provoke its catastrophic rupture (12). Abnormal accumulation of inflammatory cells can also be observed at this portion, and these accumulated cells secrete proteolytic enzymes or cytokines to weaken the plaque surface structure (13,14). However, it is still unclear which factor is mainly responsible for the outbreak of plaque rupture.

Shear stress is one of the important physical factors in the process of atherosclerosis. Shear stress is defined as a stress produced by blood flow, which tends to cause a vessel endothelium to slide or to be deformed. The value is calculated as blood viscosity multiplied by the first derivative of flow velocity with respect to the distance from the vessel wall. It

From the Division of Cardiology, Department of Medicine and Clinical Science, Yamaguchi University Graduate School of Medicine, Yamaguchi, Japan. This work was partly supported by a grant-in-aid for scientific research of the Ministry of Education, Japan (grants 16590690 and 19590819), Health and Labour Sciences research grants: Comprehensive Research on Cardiovascular Diseases from Ministry of Health, Labour, and Welfare of Japan; and Knowledge Cluster Initiative of the Ministry of Education, Japan. This study was presented, in part, at the 54th Annual Scientific Sessions of the American College of Cardiology, Orlando, Florida, March 6–9, 2005. Drs. Fukumoto and Hiro contributed equally to this work.

Manuscript received March 7, 2007; revised manuscript received August 23, 2007, accepted October 11, 2007.

**Abbreviations and Acronyms**

ACS = acute coronary syndrome(s)
BP = blood pressure
IVUS = intravascular ultrasound

has been recognized that the portions of arterial vessels that are subjected to low shear stress are those most likely to be associated with plaque formation and remodeling (15,16). Atherosclerotic plaques are frequently located in the outer side of the bifurcation at a flow divider and in the inner curvature of vessels (15,17,18), in which shear stress is relatively low. Some ex-vivo studies have demonstrated that high shear stress may be related to plaque rupture (19). Previous studies have described the complex spatial and temporal interactions between shear stress distribution and changes in vascular anatomy (20,21). However, in-vivo evidence of such a relation is limited.

Intravascular ultrasound (IVUS) provides 2-dimensional and even 3-dimensional high-quality tomographic images of coronary plaque and the vessel wall in vivo. Krams et al. (22) proposed a method of 3-dimensional color mapping of coronary shear stress along the vessel wall by using IVUS and coronary angiography. This method is a sophisticated but complicated technique that requires tremendous time to calculate shear stress. We, thus, developed a more simplified method for color mapping the distribution of shear stress, which is a user-friendly program with less calculation time that can be performed with a personal computer and some commercially available applications. The purpose of the present study was to assess the relationship between shear stress distribution and coronary plaque rupture by means of this new color-mapping program and 3-dimensional IVUS.

## Methods

**Acquisition of IVUS images.** Twenty human ruptured coronary lesions selected from patients (15 men, 5 women; age 63 ± 7 years; range 54 to 74 years) diagnosed with ACS were imaged by IVUS (Atlantis SR pro, 2.8-F, 40-MHz, Boston Scientific Corporation/SCIMED, Maple Grove, Minnesota). These lesions were selected from proximal segments of the left anterior descending artery (n = 15) or the middle portions of the right coronary artery (n = 5). Vessel segments in which the IVUS catheter could be inserted as straight as possible (curvature radius of the IVUS catheter path >80 mm) were selected. This was ensured by angiograms that at least showed no significant bending at all throughout the observed portion of interest. The tortuous lesions in which the inserted IVUS catheter bent significantly, and the lesions associated with a significant mass of thrombus on the plaque surface, were excluded.

The transducer was withdrawn automatically using a motorized pullback device (pullback speed = 0.5 mm/s). Intravascular ultrasound images were all recorded on S-VHS videotape for off-line analysis. The images were then digitized and analyzed with commercially available software for longitudinal reconstructive IVUS image analysis (Netra IVUS, SciImage, Inc., Los Altos, California).

Ruptured plaque was defined as a lesion with a distinct cavity that communicated with the lumen accompanied by a residual fibrous cap fragment. Although the sensitivity or specificity of IVUS to identify areas of plaque rupture is not validated (American College of Cardiology/American Heart Association guidelines [23]), the plaques we selected had a distinct rupture site that was readily detected, and required the agreement of 2 independent experienced observers. The lesions observed were considered as the culprit lesion, which was compatible with the clinical findings. Ruptured plaques were divided equally into 3 longitudinal portions with longitudinal IVUS findings: a proximal, middle (corresponding to the highest point of the raised plaque), and distal portion (Fig. 1). The middle portion was defined as the plaque portion that had the thickest part of the plaque.

**Color mapping of shear stress.** The technique of color mapping was developed by modifying the method of Krams et al. (22). The 3-dimensional lumen geometry of the vessel obtained from IVUS was first applied to define a mesh polygon structure that was subsequently used for the analysis of computational fluid dynamics. The generation of the mesh polygon was performed in 2 steps. The lumen contour was traced along the longitudinal plane images of 3-dimensional IVUS, by referring to cross-sectional views. The same procedure was done by revolving the plane in increments of 10 degrees (a total of 36 longitudinal luminal contour images) (Fig. 2) around the axis to the centerline of the IVUS catheter. Since it was hard to image the whole contour of side branches with the IVUS catheter inserted through the main vessel, we just measured the diameter and the bifurcation angle of each side branch at the bifurcated portion. We then straightened the lumen of the side branch over at least 100 mm, which would not affect the shear stress calculation along the main vessel. At the ruptured portion, the tracing of the luminal edge of the residual fibrous cap

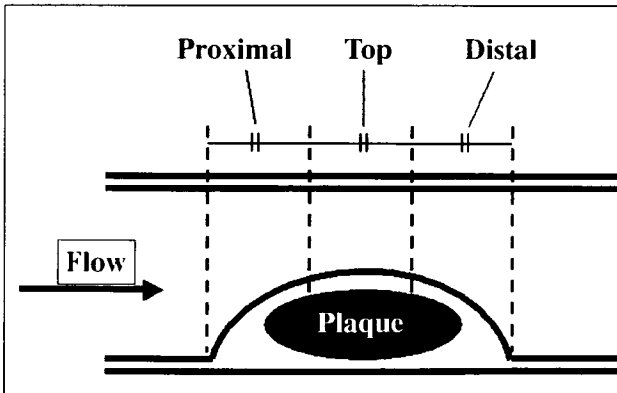


**Figure 1** **Classification of Plaque Rupture Sites**

The plaque from the proximal shoulder to the distal shoulder was divided into 3 equal parts in the longitudinal direction.

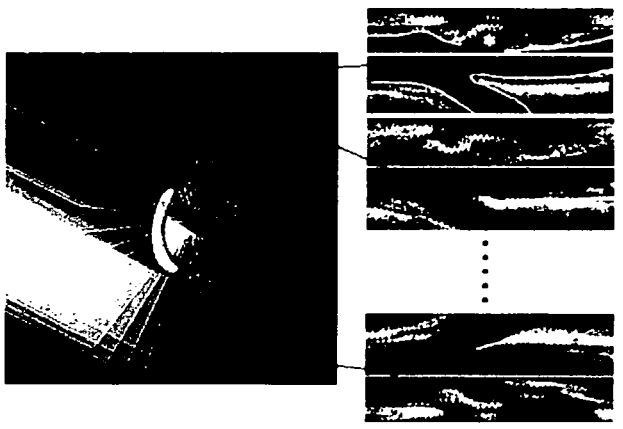

**Figure 2** **Reconstruction of the Coronary Lumen Contour**

The lumen contours traced from a total of 18 longitudinal intravascular ultrasound images while revolving the plane in increments of 10° were used to reconstruct the whole profile of the coronary lumen. These data were exported into the program of shear stress calculation. At the rupture site, the contour was extrapolated at the orifice of the ulceration cavity (*).

was smoothly extrapolated to reconstruct the luminal contour before the rupture. When the cap was too deformed to trace, the lesion was excluded. To assure that one can reasonably extrapolate the original contour of a plaque by connecting the dots between the edges of the craters, ruptured plaques with a significant amount of residual fibrous cap, which did not have unnatural cambers, were selected. The 3-dimensional luminal contour was then transferred to a commercially available program to create a mesh polygon structure (Pro-modeler 2003, CD-Adapco Japan, Kanagawa, Japan). The data were then used to conduct a computational stress analysis using the finite element model for the purpose of color mapping of the shear stress distribution along the plaque surface.

The computational fluid dynamics analysis was performed using a commercially available application (Star LT, CD-Adapco Japan) to calculate the distribution of the velocity and the directional vector of the blood stream inside the lumen, the blood pressure (BP), and the shear stress on the plaque surface. The shear stress at the lumen surface of the artery was calculated as the product of viscosity and the gradient of blood velocity at the wall. A color mapping of the shear stress distribution was then performed. The spatial resolution of the subunits was approximately 0.01 $mm^2$. The structure was automatically meshed with 4-noded trilateral plane-strain elements. In this calculation, several assumptions were made as follows: 1) the flow was a constant laminar one; 2) there was a uniform stationary inflow velocity of 30 cm/s at the entrance of the vessel; 3) there was no flow resistance at the outlet; 4) there was no flow "slip" on the vessel wall. The detailed intravascular flow characteristics were obtained by solving the transport equations governing the conservation of mass and momentum (24). We also assumed that the arterial wall was solid and that the blood was incompressible, homogeneous, and Newtonian (25) with a density of 1,050 $kg/m^3$ and a viscosity of 0.003 PaS (26). It is said that a uniform inflow condition influences the shear stress distribution at least for 2 diameter lengths downstream and could thus also influence the shear stress distribution at the plaque side. The plaques analyzed were located at least 3 diameter lengths far away from the inflow entrance. When there is a flow divider in the vessel observed, the flow towards each branch was prorated according to the value of the inlet cross-sectional area (27).

This study was approved by the Institutional Review Board of the Hospital of Yamaguchi University School of Medicine (H18-11).

**Statistical analysis.** Values were expressed as the mean ± standard deviation. The location of the focal elevation of shear stress and the ruptured portion were classified into the proximal, the middle, and the distal portions along the longitudinal plaque surface. The kappa statistics method was used to assess the measure of agreement in this classification between the location of rupture and the location of the focal elevation of shear stress or pressure. This method does not require any assumption that there is a correct diagnosis. The value of kappa ranges from −1.0 to +1.0. A value of 0 indicates chance agreement, whereas a value of +1.0 shows perfect agreement. A negative value indicates that disagreement is predominant among observers. A value >0.75 implies excellent agreement, values from 0.40 through 0.75 suggest fair-to-good agreement, and values less than 0.4 imply poor agreement (28).

## Results

Among the 20 patients selected, 15 had acute myocardial infarction and 5 had unstable angina. No cases had previous ACS or any coronary intervention. The mean percentage of stenosis at the atherosclerotic plaque of interest was 67.6 ± 18.0% by angiography. The mean percentage of stenotic area at the ruptured site and the maximum percentages of stenosis around the plaque in IVUS were 70.0 ± 8.4% and 79.7 ± 7.4%, respectively.

**Characteristic IVUS profile of ruptured plaque.** The echo-intensity of ruptured plaques was generally low (n = 19 of 20: 95%). The calcification was observed near but not directly adjacent to the ulcerative plaque cavity (n = 17 of 20: 85%). Deep calcification was frequently observed (n = 15 of 20: 75%), whereas superficial calcification around the rupture site was detected only in 3 cases. Intravascular ultrasound revealed that 13 plaques were ruptured at the proximal portion, and 7 were ruptured at the top or middle portions. No rupture occurred at the distal portion of the plaque.

**BP and shear stress distribution.** The calculated blood wall pressure was 82 ± 18 mm Hg. In the color mapping, several specific areas that had a localized elevation of shear stress or BP were clearly revealed. The localized elevation of

JACC Vol. 51, No. 6, 2008
February 12, 2008:645–50

shear stress or BP was defined as a clearly visualized and localized spotty elevation of shear stress. The highest value of shear stress divided by the lowest one within the whole plaque surface was more than 7.4 in all subjects.

Representative examples are shown in Figure 3 and 4. The BP was elevated focally at the proximal portions in only 2 plaques (10%), and was not elevated in any specific area in 18 plaques (90%), although an overall longitudinal gradation of the pressure was observed along the vessel wall. In these cases, the BP was uniformly or smoothly distributed without any clearly visualized focal elevation. However, the shear stress was focally elevated at the proximal portions in 12 plaques (60%), at the middle portions in 8 plaques (40%), and not at all at the distal portions. The focal elevation of shear stress was significantly matched with the rupture location (kappa = 0.79).

## Discussion

In the present study, a color mapping of the shear stress by use of a simplified computational analysis from 3-dimensional IVUS plaque images revealed that a localized elevation of shear stress on the plaque surface was related to coronary plaque rupture. This is the first in-vivo documentation visually demonstrating a relationship between shear stress distribution and the location of plaque rupture. Although the calculation of shear stress in this study used a number of assumptions, our findings suggest that this method of color mapping the shear stress along the plaque surface might be a useful tool for predicting plaque rupture sites.

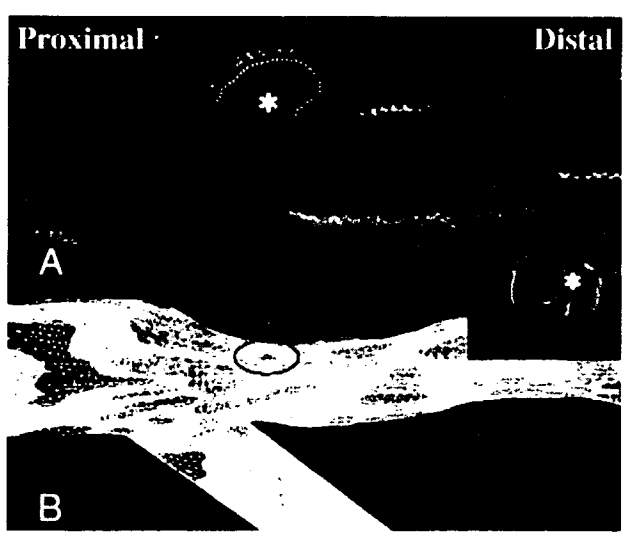


**Figure 3** **Representative Case 1: The LAD of a 60-Year-Old Man With UA**

**(A)** The longitudinal intravascular ultrasound image. Plaque rupture was observed at the proximal site of the plaque. **(B)** Color mapping of the shear stress distribution. A localized elevation of shear stress was observed on the plaque surface **(circle)**. This portion corresponded to the rupture site **(*)**. LAD = left anterior descending coronary artery; UA = unstable angina.

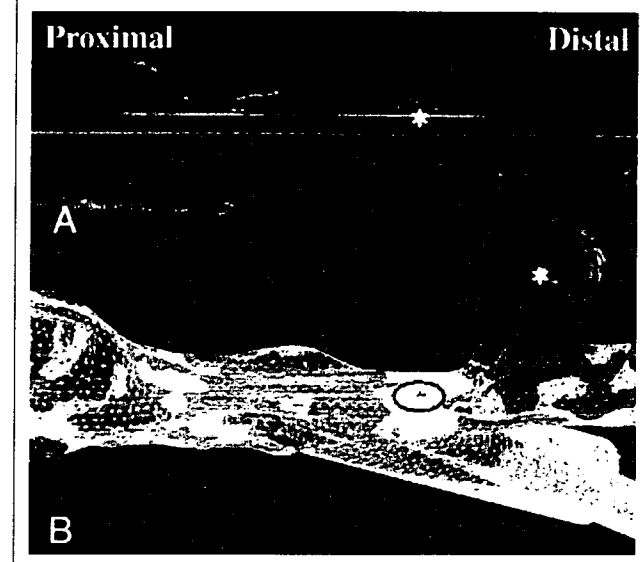


**Figure 4** **Representative Case 2: The LAD of a 57-Year-Old Man With AMI**

**(A)** The longitudinal intravascular ultrasound image. Plaque rupture was observed at the proximal site of the plaque. **(B)** A focal elevation of shear stress was observed on the plaque surface **(circle)**. This portion corresponded to the rupture site **(*)**. AMI = acute myocardial infarction; LAD = left anterior descending coronary artery.

**Plaque rupture and shear stress.** It is generally thought that a specific cluster of plaques, referred to as vulnerable plaques, is likely to exist, and numerous efforts in plaque imaging are now being concentrated on how to accurately predict the location of plaque rupture. It has been shown in pathological studies that plaque rupture frequently occurs in a noncalcified eccentric atherosclerotic plaque with nonsevere stenosis (3,4), expansive remodeling (29,30), a thin fibrous cap (3,5–7), a large lipid core (3,5,6,8,9), macrophage infiltration (7,10), spotty calcifications (11), and lack of a massive superficial calcification (31,32). However, such plaques can usually be observed at multiple nonculprit sites in the same patient with ACS (33,34). Therefore, there might be more specific triggering factors that finally provoke the plaque rupture at a particular site.

Previous studies have suggested that an excessive concentration of tensile stress within plaque may be one of the triggers of plaque rupture. When the tensile stress becomes greater than the fragility of the plaque surface, a catastrophic process of plaque rupture may be initiated. The tensile stress is increased by development of a lipid core, thinning of the fibrous cap, augmentation of plaque eccentricity (3–10, 29,30), and positive remodeling (31), whereas the fragility of plaque is aggravated by infiltration of inflammatory cells that secrete various proteinases and cytokines (13,14). In previous studies, shear stress was not considered as an important initiator of plaque rupture, because the absolute value of shear stress is negligibly low compared with the tensile stress. Therefore, the direct relationship between

shear stress and plaque rupture had not been extensively investigated, although there have been a number of studies assessing the effect of shear stress on plaque formation, or on the progression of plaque vulnerability (15,16). It is possible that the process of promoting the progression of atherosclerosis is quite different from that of initiating plaque rupture.

Shear stress is calculated as blood viscosity multiplied by the first derivative of flow velocity with respect to the distance from the vessel wall. Since the blood viscosity cannot be readily changed throughout a conduit vessel, the flow velocity gradient along the cross-sectional lumen diameter is an important factor to determine the value of the shear stress. When there is a prominent plaque hill inside a vessel lumen, the gradient is theoretically higher along the proximal part of the hill than along the distal one. Previous studies have demonstrated that plaque rupture is frequently observed at the proximal plaque portion (19), which was also shown in our study. Although spatial colocalization is not evidence of causality, our in-vivo results might support the idea that the plaque portion with high shear stress is prone to rupture.

Another interpretation suggested by our results is that "a localized elevation" of shear stress might be related to plaque rupture. A planimetric study of the macrophage contents in carotid plaques showed that macrophage-rich areas are more likely to be formed in the upstream shoulder than in the downstream shoulder of the same atherosclerotic lesion (19). Further, a previous in-vitro study by Gertz et al. (9) found that the calculated hemodynamic wall shear stress at the site of arterial narrowing was sufficiently strong to cause marked endothelial damage followed by platelet deposition and thrombus formation on exposed subendothelial tissues. Therefore, our study suggests that an elevation of shear stress in a limited area yields a significant heterogeneity in such endothelial damage, which, in turn, provokes a spiral catastrophic cascade leading to plaque rupture. Recently, Slager et al. (35) published a systematic review of the role of high shear stress as a key biological factor in provoking plaque destabilization. It has been proposed that high shear stress might stimulate endothelial cells to produce plasmin, nitric oxide, and transforming growth factor-beta, which are related to the degradation of proteoglycan matrix and/or the suppression of matrix production by smooth-muscle cells.

**Clinical implications.** A variety of factors may play a role in the initiation of plaque rupture, including tensile stress (31), turbulent pressure fluctuations (36), transient compression (37), sudden increase in intraluminal pressure (38), rupture of the vaso vasorum (39), material fatigue (3,8), and cellular inflammatory reactions (3,10). This study suggests that assessment of the shear stress within a plaque along the longitudinal axis of a vessel is also important for identifying vulnerable plaques. This approach may help identify vulnerable plaques or even help predict the point of future rupture.

**Study limitations.** In this study, in order to calculate the shear stress as accurately as possible, we chose relatively straight coronary segments of the lumen into which the IVUS catheter could be inserted with minimal bending. However, the use of 3-dimensional IVUS images still has the potential for errors in reconstructing the lumen contour. This study was performed under the assumption that the catheter path was almost straight (curvature radius of the IVUS catheter path >80 mm). This value of 80 mm was selected based upon a validation study, which assured that the real point of shear stress concentration would not be significantly deviated from the point obtained under the assumption that the catheter path was straight.

In this study, the electrocardiogram triggering was not applied to the cross sections before image segmentation. However, the pulsatile change in vessel diameter was <5%, the effect of which might be neglected in the shear stress calculation. This study assumed that the presence of the catheter in the vessel did not alter the lumen morphology significantly.

Furthermore, the flow was considered to be laminar and Newtonian at the entry of the vessel conduit, and turbulent flow was not considered, while in-vivo coronary flow is pulsatile. This might have led to errors in calculating the shear stress. However, the most important finding is not the absolute value of the shear stress, but the distribution of the shear stress along the plaque surface. When the blood flow is turbulent, the location of the elevation of shear stress might also be changed, although the imaged plaque shape was not sufficiently tortuous to generate a turbulent flow in this study.

Another implicit assumption here is that the ruptured plaque has the same contour as the plaque before rupture. However, it should be stressed that our simplified method of shear stress color mapping could predict the location of the plaque rupture. Given the major set of simplifying assumptions as mentioned in the previous text, it is remarkable that such a high correlation between predicted and actual rupture locations was seen.

The included lesions were relatively stenotic (67% by angiography). It is well known that plaques prone to rupture are usually less stenotic. However, this study was regarding the concentration of shear stress rather than its absolute value. Therefore, if the similar concentration of shear stress can be observed even on less stenotic plaque surface, it might be extrapolated to say that such portion would provoke the plaque rupture.

## Conclusions

A color mapping of the distribution of shear stress revealed that a localized elevation of shear stress could be observed on each plaque surface, and that the location of focally elevated shear stress was frequently matched with the plaque rupture site. This in-vivo study was the first to suggest that a localized elevation of shear stress might be related to coronary plaque rupture. Furthermore, the imaging of shear stress by our method may help identify vulnerable plaques or even help predict the sites of future rupture.

**Reprint requests and correspondence:** Dr. Takafumi Hiro, Division of Cardiology, Department of Medicine and Clinical Science, Yamaguchi University Graduate School of Medicine, 1-1-1 Minami Kogushi, Ube, Yamaguchi, 755-8505, Japan. E-mail: thiro@yamaguchi-u.ac.jp.

## REFERENCES

1. Davies MJ, Thomas A. Thrombosis and acute coronary artery lesions in sudden cardiac ischemic death. N Engl J Med 1984;310:1137–40.
2. Fuster V, Badimon L, Badimon JJ, Chesebro JH. The pathogenesis of coronary artery disease and the acute coronary syndromes (1). N Engl J Med 1992;326:242–50.
3. Falk E, Shah PK, Fuster V. Coronary plaque disruption. Circulation 1995;92:657–71.
4. Little WC, Constantinescu M, Applegate RJ, et al. Can coronary angiography predict the site of a subsequent myocardial infarction in patients with mild to-moderate coronary artery disease? Circulation 1988;78:1157–66.
5. Loree HM, Kamm RD, Stringfellow RG, Lee RT. Effects of fibrous cap thickness on peak circumferential stress in model atherosclerotic vessels. Circ Res 1992;71:850–8.
6. Nissen SE, Yock P. Intravascular ultrasound: novel pathophysiological insights and current clinical applications. Circulation 2001;103:604–16.
7. Davies MJ, Richardson PD, Woolf N, Katz DR, Mann J. Risk of thrombosis in human atherosclerotic plaques: role of extracellular lipid, macrophage, and smooth muscle cell content. Br Heart J 1993;69:377–81.
8. Richardson PD, Davies MJ, Born GV. Influence of plaque configuration and stress distribution on fissuring of coronary atherosclerotic plaques. Lancet 1989;2:941–4.
9. Gertz SD, Roberts WC. Hemodynamic shear force in rupture of coronary arterial atherosclerotic plaques. Am J Cardiol 1990;66:1368–72.
10. Lendon CL, Davies MJ, Born GV, Richardson PD. Atherosclerotic plaque caps are locally weakened when macrophages density is increased. Atherosclerosis 1991;87:87–90.
11. Ehara S, Kobayashi Y, Yoshiyama M, et al. Spotty calcification typifies the culprit plaque in patients with acute myocardial infarction: an intravascular ultrasound study. Circulation 2004;110:3424–9.
12. Cheng GC, Loree HM, Kamm RD, Fishbein MC, Lee RT. Distribution of circumferential stress in ruptured and stable atherosclerotic lesions. A structural analysis with histopathological correlation. Circulation 1993;87:1179–87.
13. van der Wal AC, Becker AE, van der Loos CM, Das PK. Site of intimal rupture or erosion of thrombosed coronary atherosclerotic plaques is characterized by an inflammatory process irrespective of the dominant plaque morphology. Circulation 1994;89:36–44.
14. Shah PK, Falk E, Badimon JJ, et al. Human monocyte-derived macrophages induce collagen breakdown in fibrous caps of atherosclerotic plaques. Potential role of matrix-degrading metalloproteinases and implications for plaque rupture. Circulation 1995;92:1565–9.
15. Asakura T, Karino T. Flow patterns and spatial distribution of atherosclerotic lesions in human coronary arteries. Circ Res 1990;66:1045–66.
16. Ku DN, Giddens DP, Zarins CK, Glagov S. Pulsatile flow and atherosclerosis in the human carotid bifurcation. Positive correlation between plaque location and low oscillating shear stress. Arterioscle rosis 1985;5:293–302.
17. Sacks FM, Pasternak RC, Gibson CM, Rosner B, Stone PH. Effect on coronary atherosclerosis of decrease in plasma cholesterol concentrations in normocholesterolaemic patients. Harvard Atherosclerosis Reversibility Project (HARP) group. Lancet 1994;344:1182–6.
18. Malek AM, Alper SL, Izumo S. Hemodynamic shear stress and its role in atherosclerosis. JAMA 1999;282:2035–42.
19. Dirksen MT, van der Wal AC, van den Berg FM, van der Loos CM, Becker AE. Distribution of inflammatory cells in atherosclerotic plaques relates to the direction of flow. Circulation 1998;98:2000–3.
20. Wentzel JJ, Janssen E, Vos J, et al. Extension of increased atherosclerotic wall thickness into high shear stress regions is associated with loss of compensatory remodeling. Circulation 2003;108:17–23.
21. Stone PH, Coskun AU, Kinlay S, et al. Effect of endothelial shear stress on the progression of coronary artery disease, vascular remodeling, and in-stent restenosis in humans: in vivo 6 month follow up study. Circulation 2003;108:438–44.
22. Krams R, Wentzel JJ, Oomen JA, et al. Evaluation of endothelial shear stress and 3D geometry as factors determining the development of atherosclerosis and remodeling in human coronary arteries in vivo. Combining 3D reconstruction from angiography and IVUS (ANGUS) with computational fluid dynamics. Arterioscler Thromb Vasc Biol 1997;17:2061–5.
23. Mintz GS, Nissen SE, Anderson WD, et al. ACC clinical expert consensus document on standards for acquisition, measurement and reporting of intravascular ultrasound studies: a report of the American College of Cardiology Task Force on Clinical Expert Consensus Documents (Committee to Develop a Clinical Expert Consensus Document on Standards for Acquisition, Measurement and Reporting of Intravascular Ultrasound Studies [IVUS]). J Am Coll Cardiol 2001;37:1478–92.
24. Ilegbusi OJ, Hu Z, Nesto R, et al. Determination of blood flow and endothelial shear stress in human coronary artery in vivo. J Invasive Cardiol 1999;11:667–74.
25. Friedman MH, Bargeron CB, Duncan DD, Hutchins GM, Mark FF. Effects of arterial compliance and non Newtonian rheology on correlations between intimal thickness and wall shear. J Biomech Eng 1992;114:317–20.
26. Krijger JK, Heethaar RM, Hillen B, Hoogstraten HW, Ravensbergen J. Computation of steady three dimensional flow in a model of the basilar artery. J Biomech 1992;25:1451–65.
27. Mittal N, Zhou Y, Linares C, et al. Analysis of blood flow in the entire coronary arterial tree. Am J Physiol Heart Circ Physiol 2005;289:H439–46.
28. Fleiss JL. The measurement of interrater agreement. In: Statistical Methods for Rates and Proportions. New York, NY: John Wiley, 1981:212–36.
29. Schoenhagen P, Ziada KM, Kapadia SR, Crowe TD, Nissen SE, Tuzcu EM. Extent and direction of arterial remodeling in stable versus unstable coronary syndromes: an intravascular ultrasound study. Circulation 2000;101:598–603.
30. von Birgelen C, Klinkhart W, Mintz GS, et al. Plaque distribution and vascular remodeling of ruptured and nonruptured coronary plaques in the same vessel: an intravascular ultrasound study in vivo. J Am Coll Cardiol 2001;37:1864–70.
31. Imoto K, Hiro T, Fujii T, et al. Longitudinal structural determinants of atherosclerotic plaque vulnerability: a computational analysis of stress distribution using vessel models and three-dimensional intravascular ultrasound imaging. J Am Coll Cardiol 2005;46:1507–15.
32. Raggi P, Callister TQ, Cooil B, et al. Identification of patients at increased risk of first unheralded acute myocardial infarction by electron beam computed tomography. Circulation 2000;101:850–5.
33. Hong MK, Mintz GS, Lee CW, et al. Comparison of coronary plaque rupture between stable angina and acute myocardial infarction: a three vessel intravascular ultrasound study in 235 patients. Circulation 2004;110:928–33.
34. Kotani J, Mintz GS, Castagna MT, et al. Intravascular ultrasound analysis of infarct-related and non-infarct-related arteries in patients who presented with an acute myocardial infarction. Circulation 2003;107:2889–93.
35. Slager CJ, Wentzel JJ, Gijsen FJ, et al. The role of shear stress in the destabilization of vulnerable plaques and related therapeutic implications. Nat Clin Pract Cardiovasc Med 2005;2:456–64.
36. Loree HM, Kamm RD, Atkinson CM, Lee RT. Turbulent pressure fluctuations on surface of model vascular stenoses. Am J Physiol 1991;261:H644–50.
37. Binns RL, Ku DN. Effect of stenosis on wall motion. A possible mechanism of stroke and transient ischemic attack. Arteriosclerosis 1989;9:842–7.
38. Muller JE, Tofler GH, Stone PH. Circadian variation and triggers of onset of acute cardiovascular disease. Circulation 1989;79:733–43.
39. Barger AC, Beeuwkes R, 3rd, Lainey LL, Silverman KJ. Hypothesis: vasa vasorum and neovascularization of human coronary arteries. A possible role in the pathophysiology of atherosclerosis. N Engl J Med 1984;310:175–7.

*Am J Physiol Heart Circ Physiol* 294: H1164–H1173, 2008.
First published December 7, 2007; doi:10.1152/ajpheart.00960.2007.

# Altered expression of connexin43 contributes to the arrhythmogenic substrate during the development of heart failure in cardiomyopathic hamster

**Takashi Sato,[1]* Tomoko Ohkusa,[1]* Haruo Honjo,[2] Shinsuke Suzuki,[1] Masa-aki Yoshida,[1] Yuko S. Ishiguro,[2] Harumichi Nakagawa,[2] Masatoshi Yamazaki,[2] Masafumi Yano,[1] Itsuo Kodama,[2] and Masunori Matsuzaki[1]**

[1]*Division of Cardiology, Department of Medicine and Clinical Science, Yamaguchi University Graduate School of Medicine, Yamaguchi; and* [2]*Department of Cardiovascular Research, Research Institute of Environmental Medicine, Nagoya University, Nagoya, Japan*

Submitted 17 August 2007; accepted in final form 6 December 2007

**Sato T, Ohkusa T, Honjo H, Suzuki S, Yoshida M, Ishiguro YS, Nakagawa H, Yamazaki M, Yano M, Kodama I, Matsuzaki M.** Altered expression of connexin43 contributes to the arrhythmogenic substrate during the development of heart failure in cardiomyopathic hamster. *Am J Physiol Heart Circ Physiol* 294: H1164–H1173, 2008. First published December 7, 2007; doi:10.1152/ajpheart.00960.2007.— Heart failure is known to predispose to life-threatening ventricular tachyarrhythmias even before compromising the systemic circulation, but the underlying mechanism is not well understood. The aim of this study was to clarify the connexin43 (Cx43) gap junction remodeling and its potential role in the pathogenesis of arrhythmias during the development of heart failure. We investigated stage-dependent changes in Cx43 expression in UM-X7.1 cardiomyopathic hamster hearts and associated alterations in the electrophysiological properties using a high-resolution optical mapping system. UM-X7.1 hamsters developed left ventricular (LV) hypertrophy by ages 6~10 wk and showed a moderate reduction in LV contractility at age 20 wk. Appreciable interstitial fibrosis was recognized at these stages. LV mRNA and protein levels of Cx43 in UM-X7.1 were unaffected at age 10 wk but significantly reduced at 20 wk. The expression level of Ser255-phosphorylated Cx43 in UM-X7.1 at age 20 wk was significantly greater than that in control golden hamsters at the same age. In UM-X7.1 at age 10 wk, almost normal LV conduction was preserved, whereas the dispersion of action potential duration was significantly increased. UM-X7.1 at age 20 wk showed significant reduction of cardiac space constant, significant decrease in conduction velocity, marked distortion of activation fronts, and pronounced increase in action potential duration dispersion. Programmed stimulation resulted in sustained ventricular tachycardia or fibrillation in UM-X7.1. LV activation during polymorphic ventricular tachycardia was characterized by multiple phase singularities or wavebreaks. During the development of heart failure in the cardiomyopathic hamster, alterations of Cx43 expression and phosphorylation in concert with interstitial fibrosis may create serious arrhythmogenic substrate through an inhibition of cell-to-cell coupling.

cardiomyopathy; ventricular arrhythmia; optical mapping; phosphorylation

LIFE-THREATENING VENTRICULAR tachyarrhythmias often occur in patients with heart failure even at a compensated stage (6). The underlying mechanisms are not well understood. In the heart, gap junctions provide the pathway for intercellular current flow, enabling coordinated action potential propagation and contraction. Gap junction channels are constructed from connexins (Cxs), a multigene family of conserved proteins. To date, the connexin (Cx) gene family comprises 20 members in the mouse and 21 members in the human genome. In the mammalian heart, the following Cxs have been identified: Cx37, Cx40, Cx43, and Cx45 (30). In adult ventricular muscle, cell-to-cell coupling is provided predominantly by Cx43 channels and to a lower extent by Cx45 (11, 19, 31). Newly synthesized Cx43 disappears rapidly with a half-life of only 2.5~5.0 h, and its function is regulated by phosphorylation (30). Consequently, dynamic turnover of Cxs in the heart may be an important mechanism modulating intercellular coupling and impulse propagation. There are several phosphorylation sites in Cx43, and the functional consequence of phosphorylation is variable. The phosphorylation of Cx43 on Ser255 has been shown to cause gap junctional uncoupling in cultured cell lines (40). In many recent studies (4, 5, 8, 9, 15, 19, 20, 27, 29, 31, 38, 39, 43, 44), altered expression, organization, and phosphorylation of the Cx43 in ventricular muscle has been demonstrated in human patients as well as animal models of diverse heart diseases, including ischemic, hypertrophic, and tachycardia-induced cardiomyopathy, and genetically engineered animals. Such gap junction remodeling is supposed to contribute to the abnormal conduction properties and arrhythmias in the ventricle under these pathological conditions. As to idiopathic cardiomyopathy, however, the available information is still limited and much remains to be clarified. The present study was designed to shed light on this issue.

We used a strain of the Syrian cardiomyopathic hamster, UM-X7.1 (a derivative of the BIO14.6 strain), since its characteristic features of heart failure progression have been demonstrated in previous studies (36, 37); the animals show moderate compensated left ventricular (LV) contractile dysfunction at ages 10~20 wk and serious decompensated heart failure at ages beyond ~24 wk. In the present study, we investigated stage-dependent changes in Cx43 expression in UM-X7.1 at ages 6~20 wk. Associated alterations in the electrophysiological properties and propensities for life-threatening arrhythmias were also investigated using a high-resolution optical mapping system. The results reveal that UM-X7.1 hamsters at age 20 wk, compared with golden hamsters (controls), exhibit a significant reduction in Cx43 expression (mRNA and protein) and moderate interstitial fibrosis. Interestingly, the proportion of

* T. Sato and T. Ohkusa contributed equally to this work.

Address for reprint requests and other correspondence: T. Ohkusa, Division of Cardiology, Dept. of Medicine and Clinical Science, Yamaguchi Univ. Graduate School of Medicine, 1-1-1, Minami-kogushi, Ube, Yamaguchi 755-8505, Japan (e-mail: ohkusa@yamaguchi-u.ac.jp).

The costs of publication of this article were defrayed in part by the payment of page charges. The article must therefore be hereby marked "*advertisement*" in accordance with 18 U.S.C. Section 1734 solely to indicate this fact.

the Ser255-phosphorylated form of Cx43 is increased compared with control animals at the same age. This gap junction remodeling is accompanied by reduced electrical cell-to-cell coupling, serious distortions in conductivity, repolarization inhomogeneity, and an increased propensity for ventricular tachycardia/fibrillation (VT/VF).

## MATERIAL AND METHODS

*Animal model.* UM-X7.1 cardiomyopathic hamsters (kindly provided by Dr. Lemanskie, SUNY Health Science Center, Syracuse, NY, and inbred in our laboratory) and sex- and age-matched normal golden hamsters (control, Japan SLC, Hamamatsu, Japan) were used as experimental animals. All animal procedures were approved by the Yamaguchi University Experimental Animal Care and Use Committee. The investigation conforms with the *Guide for Care and Use of Laboratory Animals* published by the US National Institute of Health (NIH Publication No. 85-23, revised 1996).

*Echocardiography, electrocardiography, and histology.* Echocardiography was performed using an echocardiograph model SSD-1000, with a 10-MHz sector scan probe (Aloka, Tokyo, Japan). Left ventricular end-diastolic diameter (LVEDd), left ventricular end-systolic diameter (LVESd), and fractional shortening (FS) were calculated according to a standard formula, as applied in our previous studies (36, 37). ECGs were recorded using a PowerLab System (AD Instruments, Colorado Springs, CO) for 24 h.

Specimens for histological examination were obtained from heart cross slices cut mid-way between the apse and base. The samples were embedded in paraffin, and 4-μm thick sections were cut and stained. The connective-tissue volume-fraction was assessed with the aid of Azan staining and calculated as previously described (37).

*RT-PCR amplification.* Total ventricular RNA was isolated from frozen cell samples by the acid guanidinium thiocyanate/phenol/chloroform extraction method (25). cDNA was prepared using a Takara RNA PCR kit (Takara, Tokyo, Japan; Ref. 26). The primers for the amplification of Cx43 and GAPDH were designed from published sequences (35). For Cx43, they were based on hamster sequences (GenBank accession no. AY206455): sense primer, 5′-GGC CTG CTA AGA ACC TAC ATC ATC AGT-3′; and antisense primer, 5′-GCA ATC GAG TGG CGT CTT GAT GCT CAA-3′. For GAPDH, they were based on rat sequences: sense primer, 5′-CTT CAT TGA CCT CAA CTA CAT GGT-3′; and antisense primer, 5′-CTC AGT GTA GCC CAG GAT GCC CTT-3′. The GAPDH gene product was used as an internal control, since it is still used widely in the molecular biology literature despite some controversy (33). In the present experiments, there were no significant differences in the absolute amount of GAPDH mRNAs among the data groups.

*Immunoblotting, immunohistochemistry, and confocal microscopy.* For immunoblotting, LV tissues were lysed with lysis buffer (150 mmol/l NaCl, 100 mmol/l $Na_3VO_4$, 1.5 mmol/l $MgCl_2$, 50 mmol/l NaF, 50 mmol/l HEPES, 1 mmol/l EGTA, 10% glycerol, 1 mmol/l PMFS, 1% Triton X-100, and 10 μg/ml leupeptin, pH 7.5), and the tissue extracts were electrophoresed in SDS-polyacrylamide gels as previously described (18). The following primary antibodies were used: rabbit anti-Cx43 antibody (1:1,000; catalog number 71-0700, Zymed, San Francisco, CA); mouse anti-Cx45 antibody (1:100; Chemicon International, Temecula, CA); rabbit anti-p-Cx43 (Ser255) antibody (1:200; sc12899R, Santa Cruz Biotechnology, Santa Cruz, CA); rabbit anti-p-Cx43 (Tyr265) antibody (1:200; sc17220R, Santa Cruz Biotechnology); and monoclonal anti-GAPDH antibody (1:1,000; Clone GAPDH-71.7, Sigma, St. Louis, MO). The amount of protein recognized by the antibodies was quantified by means of an enhanced chemiluminescence immunoblotting detection system (Amersham, Buckinghamshire, England).

In the immunohistochemistry, three different primary antibodies for Cx43 were used. Rabbit anti-Cx43 antibody (1:100, see Fig. 4; catalog number 71-0700, Zymed) or mouse anti-Cx43 antibody (1:100, for double staining, see Fig. 5; Transduction Laboratories, Newington, NH) to recognize total Cx43 (both phosphorylated and nonphosphorylated), and rabbit anti-p-Cx43 (Ser255) antibody (1:100; sc12899R; Santa Cruz Biotechnology) to recognize specifically Ser255-phosphorylated Cx43. After permeabilization (0.1% Triton X-100), quenching, and blocking (10% goat serum), samples were incubated with the respective antibody (1:100) overnight at room temperature. Primary antibody-bound Cx43 and p-Cx43 (Ser255) were visualized by FITC-conjugated anti-rabbit (for anti-Cx43 antibody, see Fig. 4) or anti-mouse (for anti-Cx43 antibody for double staining, see Fig. 5) IgG, and TRITC-conjugated anti-rabbit IgG for anti-p-Cx43 (Ser255), respectively, and examined using a confocal microscope (LSM510, Zeiss). The proportion of Cx43 immunoreactive signal was defined as the number of high signal-intensity (>90% of the maximum level) pixels divided by the total number of pixels occupied by the myocytes (44). Ten individual measurements in different fields were averaged to yield a single value for each slide.

*Optical action potential mapping.* We used a high-resolution optical mapping system to examine the electrophysiological properties of the heart. Details of the system and mapping procedure were described in our previous studies (2, 42). In brief, isolated hamster hearts were continuously perfused on a Langendorff apparatus with modified Krebs-Ringer solution equilibrated with 95% $O_2$-5% $CO_2$ (37°C, pH 7.4). The hearts were stained with the voltage-sensitive dye 4-{β-[2-(di-*n*-butylamino)-6-naphthyl]vinyl}pyridinium (di-4-ANEPPS). To minimize motion artifacts, 15 mmol/l of 2,3-butandione monoxime were added. The heart was illuminated with bluish light-emitting diodes; the emitted fluorescence was recorded with a solid-state image-sensing digital video camera (Fastcam-Max, Photron) to acquire 10-bit gray scale images from 256 × 256 sites simultaneously at a speed of 1,000 frames/s. The image acquired (15 × 15 mm) covered the antero-lateral surface of the LV and part of the anterior surface of the right ventricle (RV), yielding a spatial resolution at 0.06 mm per pixel.

The background fluorescence was subtracted from each frame to reveal the signal. The fluorescence signals were inverted and then averaged to reduce noise. Spatial resolution after the long-pass filtering was 0.18–0.24 mm. Isochrone maps were generated from the filtered image. To analyze action potential configuration, a five-point time median filter was applied to the spatially averaged data (23), and then the data were normalized to within the range of the maximum and the minimum values in the respective 1,000 frames sampled. A point at 10% depolarization in the upstroke phase and a time point at 90% repolarization were identified, and their interval was measured as the action potential duration at 90% repolarization ($APD_{90}$). The dispersion of $APD_{90}$ values in the recording area was displayed as color gradient maps with 1.0-ms steps ranging from red (the shortest) to blue (the longest). The pattern of wave propagation during VT/VF was quantified using the phase mapping method described by Gray et al. (13). Phase singularity (PS) was defined as the point at which all phases converged.

Conduction velocity (CV) was measured during constant stimulation (S1) at the center of the LV free wall at a basic cycle length of 200 ms. The CV was measured in a central 6 × 6-mm square around the stimulation site, as measurement in the outer periphery would be hampered by the sharp curvature of the ventricular surface. The longitudinal (L) direction of propagation was determined from the activation map so that it crossed the most widely spaced isochrones. A second line for transverse (T) direction of propagation was drawn perpendicular to the first line through the densely spaced isochrone. The CVs in the L ($CV_L$) and T ($CV_T$) directions were calculated from the slope of a linear least-square fit of the activation time plotted against the distance. Data from an area very close to the stimulation site (<1.0 mm) were excluded to minimize the virtual electrode polarization effects.

APD and its distribution were measured under similar constant stimulation at the apex. The pulses applied were 2.0 ms in duration at an intensity 1.3 times the threshold. We used a premature stimulation

protocol to induce VT/VF. After rapid stimulation at a S1-S1 interval of 150 ms, a single premature stimulation (S2) was applied at the center of the anterior LV free wall, and the sequence was repeated by progressive shortening of the S1-S2 interval. Widely spaced bipolar electrograms were recorded between the apex of the LV and the high lateral wall of the RV to monitor the whole ventricular excitation.

*Measurement of intercellular electrical coupling.* Intercellular electrical coupling was assessed by optically measuring overall tissue resistivity in the LV of Langendorff-perfused hearts according to the methods originally described by Akar et al. (3): spatial decay of transmembrane potential in response to subthreshold depolarizing stimuli was measured with the use of the high-resolution optical mapping system, and the space constant ($\lambda$) was determined by fitting of the data with a single exponential function. In these experiments, magnified fluorescence images (covering 5 × 5 mm, 256 × 256 pixels) were obtained through a photographic lens with a longer focal distance (Micro-Nikkor 105 mm f/2.8D, Nikon) at a sampling rate of 0.5 Hz. A single cathodal subthreshold stimulus (20 ms in duration, ~0.8 times threshold) was delivered during electrical diastole after regular (250- to 400-ms intervals) suprathreshold stimuli (2.0 ms in duration, ~1.2 times diastolic threshold) through a Teflon-coated platinum electrode (100 μm in diameter) placed at the center of the anterior LV free wall. To induce subthreshold membrane potential responses to such long depolarizing stimuli, myocardial excitability was reduced by an increase in the extracellular $K^+$ concentration from 5 to 8 mmol/l. Membrane responses to subthreshold stimuli were estimated as the maximum change in fluorescence intensity relative to the resting level and normalized with respect to the amplitude of baseline action potential signals at each recording site.

*Statistics.* All data are presented means ± SD. Comparisons between data were made by ANOVA. Frequency of VT/VF induction was compared by $\chi^2$-test analysis. Differences were taken to be significant at $P < 0.05$.

## RESULTS

*Somatic and cardiac growth.* The body weight of UM-X7.1 hamsters was significantly smaller at each stage than that of golden hamsters; however, the value of the LV-to-body weight ratio was significantly higher in each UM-X7.1 group (Fig. 1, *A* and *B*, $n = 5$ in each group). Mean cardiomyocyte width of UM-X7.1 hamsters was significantly greater than that in golden hamsters at ages 10~24 wk (Fig. 1*C*, $n = 5$ in each group). The connective-tissue volume-fraction of UM-X7.1 hamsters was significantly higher than that of golden hamsters (Fig. 1, *D* and *E*, $n = 5$ in each group; 5.3 ± 0.5 vs. 1.0 ± 0.2% at age 10 wk, 7.0 ± 0.5 vs. 1.9 ± 1.1% at age 20 wk, and 12.8 ± 1.5 vs. 2.5 ± 0.8% at age 24 wk).

*Echocardiography and electrocardiography.* Figure 2*A* shows representative M-mode echocardiograms of the LV at the papillary muscle level in each group of hamsters. Table 1 shows serial changes in LV dimensions and FS in UM-X7.1 and golden hamster groups ($n = 5$ in each group). At age 20 wk, LVEDd and LVESd were significantly greater and FS was significantly lower in UM-X7.1 hamsters than those in golden hamsters. Figure 2*B* shows representative ECGs for each group. A significant prolongation in QRS and PQ duration was detected in UM-X7.1 hamsters at ages 20 and 24 wk (Fig. 2*B*, $n = 5$ in each group). These observations indicate that UM-X7.1 hamsters develop cardiac hypertrophy with interstitial fibrosis at age 10 wk and suffered from cardiac dysfunction with ECG abnormality at age 20 wk and thereafter. As shown in Fig. 2*C* (Kaplan-Meier survival curve), UM-X7.1 hamsters died from congestive heart failure at over age 25 wk. Based on these results, we focused on the gap junction remodeling and its consequent electrophysiological changes during the compensated stage (ages 10~20 wk) of heart failure in UM-X7.1 cardiomyopathic hamsters.

*Cx43 expression.* To quantify Cx43 expression (mRNA and protein), RT-PCR and Western blot analysis were performed. Cx43 expression (mRNA and protein) in UM-X7.1 hamsters at age 20 wk, compared with golden hamsters, was significantly reduced by 33 and 55%, respectively (Fig. 3, *A* and *B*, $n = 5$ in each group). The total content of Cx45 in UM-X7.1 hamsters at age 20 wk did not show any difference from control hamsters (Fig. 3*C*, $n = 5$ in each group). Quantitative immunoconfocal microscopy revealed that Cx43 positive area decreased significantly in UM-X7.1 hamsters at age 10 wk (by 33%) and the reduction was more prominent at age 20 wk (by 58%) compared with golden hamsters at the corresponding age

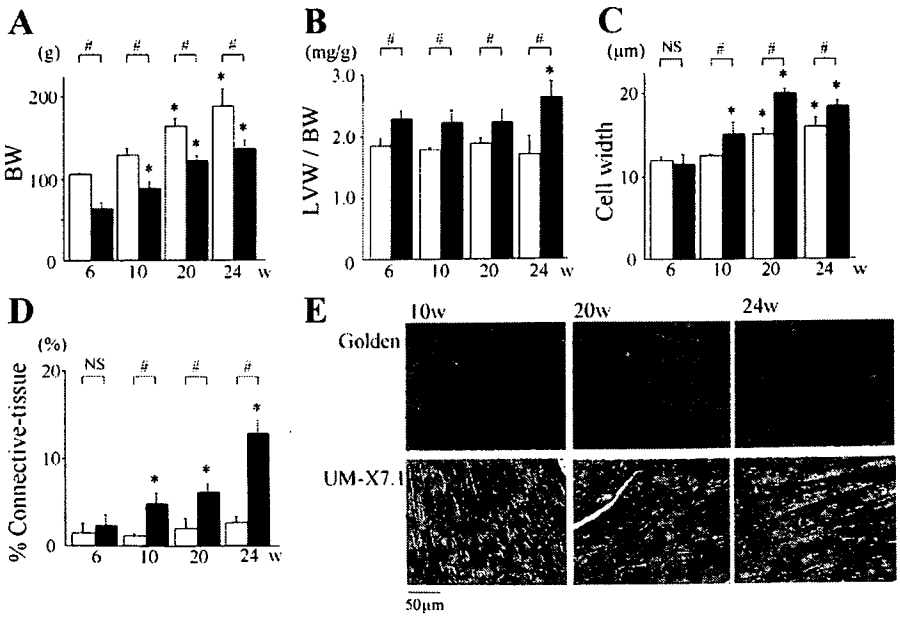


Fig. 1. Somatic and cardiac growth data and histology of golden (open bars) and UM-X7.1 (closed bars) hamsters ($n = 5$ in each group). *A*: BW, body wt; *B*: LVW/BW, left ventricular-to-body wt ratio; *C*: cell width; *D*: %connective-tissue:connective-tissue volume-fraction; *E*: representative Azan staining. *$P < 0.01$ vs. 6 wk of the same strain; #$P < 0.01$ vs. age-matched golden hamster. NS, not significant; w, week.

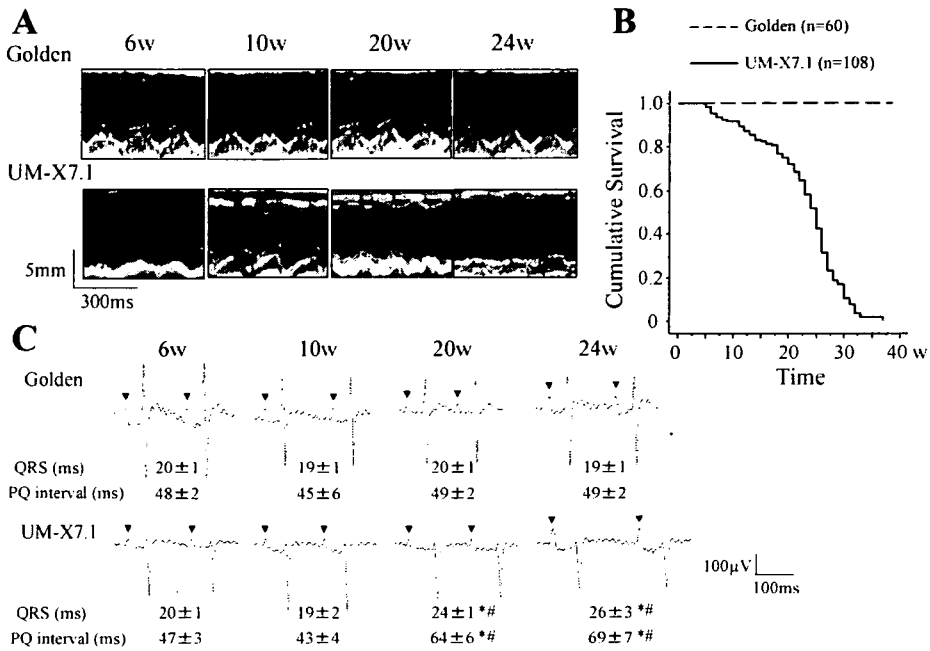


Fig. 2. M-mode echocardiograms (*A*) and ECGs (*B*) serially obtained from representative golden and UM-X7.1 hamsters. Echoes were recorded at the level of the papillary muscles. For group data ($n$ = 5 in each group), see Table 1. Mean values of QRS and the PQ interval are presented at the *bottom* of the ECG. *C*: Kaplan-Meier survival curves for golden and UM-X7.1 hamsters. Arrowhead indicates a P wave. *$P < 0.01$ vs. 6 wk of the same strain; #$P < 0.01$ vs. age-matched golden hamster.

(Fig. 4, $n$ = 5 in each group). Interestingly, the relative expression level of Ser255-phosphorylated Cx43, which has been shown in the mouse cell line to cause the downregulation of gap junctional intercellular communication (40), was markedly increased in UM-X7.1 hamsters compared with golden hamsters at age 6 wk (1.55 ± 0.19 vs. 0.96 ± 0.30, $P < 0.01$) and age 20 wk (0.83 ± 0.34 vs. 0.28 ± 0.29, $P < 0.01$; Fig. 5*A*, $n$ = 5 in each group). The relative expression level of Tyr265-phosphorylated Cx43 showed no significant difference between UM-X7.1 and golden hamsters at ages 6~20 wk (Fig. 5*B*, $n$ = 5 in each group).

Figure 5*C* shows the double staining for total Cx43 (green) and Ser255-phosphorylated Cx43 (red). In LV from golden hamsters at age 20 wk, staining for total Cx43 (green) and Ser255-phosphorylated Cx43 (red) was recognized at the cell termini. The Cx43 staining patterns of LV tissue from UM-X7.1 hamsters at age 20 wk were markedly differed from those of golden hamsters; total Cx43 staining (green) at cell termini was decreased, whereas Ser255-phosphorylated Cx43 immunolabeling was increased at cell termini (red). Positive staining for Ser255-phosphorylated Cx43 was also recognized in cytosolic areas (red). Merged images showed yellow-colored staining at the cell termini. Lateralization of Cx43 did not appear in UM-X7.1 hamsters at ages 6~20 wk.

*Electrophysiological properties and vulnerability for VT/VF.* Conduction properties were examined during constant stimulation (S1) from a center of the LV free wall. The isochrones of the activation front exhibited a smooth, symmetric, elliptical pattern in golden hamsters at ages 10 and 20 wk (Fig. 6*A*, *left*; the online version of this article contains supplemental data; see Supplemental Movie 1); the axis of the ellipse corresponded to the fiber orientation of the subepicardial cardiac muscle (data not shown). In the central 6 × 6-mm square, there was a linear correlation between activation time and distance in both the L and T directions. $CV_L$ and $CV_T$ in golden hamsters at age 10 wk were 43.9 ± 0.6 and 17.4 ± 2.3 cm/s, respectively ($n$ = 5 in each group). The anisotropic ratio ($CV_L/CV_T$) was 2.6 ± 0.5. The correlation coefficient (CC) between activation time and distance was 0.98~0.99 (Table 2). Comparable values were obtained for these parameters of conduction for golden hamsters at age 20 wk, and there were no significant age-dependent changes. In UM-X7.1 hamsters at age 10 wk, the isochrones of the activation front also showed a smooth, symmetric elliptical pattern, and all the parameters of the conduction properties ($CV_L$, $CV_T$, $CV_L/CV_T$, and CCs) were similar to those of golden hamsters (Table 2). In UM-X7.1 hamsters at age 20 wk, however, the isochrones of activation front were extremely distorted, indicating spatial inhomogeneity of propagation (Fig. 6*A*, *right*; see Supplemental Movie 2). Both $CV_L$ and $CV_T$ were significantly decreased by 35~40% compared with golden hamsters at age 20 wk (Table 2). Although $CV_L/CV_T$ was comparable, CCs, which reflect the spatial homogeneity of propagation, were significantly decreased in UM-X7.1 (Table 2).

Table 1. *Echo geometry findings and cardiac function*

| | Golden | | | | UM-X7.1 | | | |
|---|---|---|---|---|---|---|---|---|
| | 6 wk | 10 wk | 20 wk | 24 wk | 6 wk | 10 wk | 20 wk | 24 wk |
| LVEDd, mm | 4.5±0.3 | 4.8±0.1 | 4.9±0.1 | 4.8±0.1 | 4.5±0.4 | 4.8±0.2 | 5.4±0.6*‡ | 6.6±0.5*‡ |
| LVESd, mm | 3.0±0.1 | 3.3±0.2 | 3.1±0.2 | 3.2±0.3 | 3.0±0.3 | 3.2±0.2 | 4.6±0.2*‡ | 5.9±0.5*‡ |
| FS, % | 33±5 | 34±4 | 37±3 | 35±5 | 33±6 | 34±5 | 19±2*‡ | 11±2*‡ |

Values are means ± SD ($n$ = 5 in each group). LVEDd, left ventricular end-diastolic diameter; LVESd, left ventricular end-systolic diameter; FS, fractional shortening. *$P < 0.01$ vs. 6 wk of the same strain; †$P < 0.05$, ‡$P < 0.01$ vs. golden hamster.

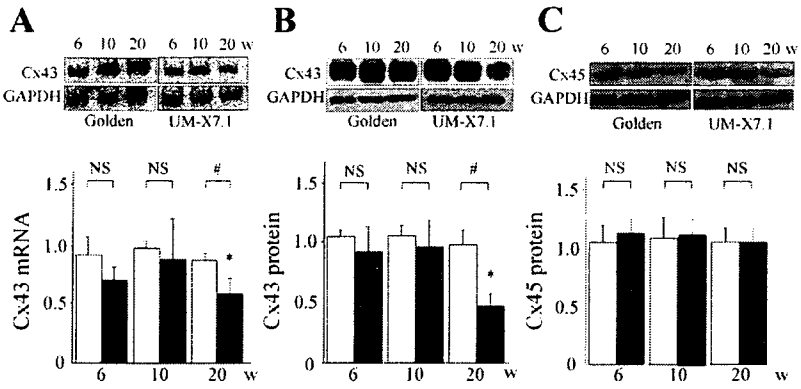


Fig. 3. Quantitative analysis of Cx43 mRNA and protein levels in left ventricular (LV) tissues ($n$ = 5 in each group). *A*: Cx43 mRNA levels estimated by RT-PCR. Amount of Cx43 mRNA was normalized to that of GAPDH. *$P < 0.05$ vs. 10 wk of the same strain; #$P < 0.05$ vs. age-matched golden hamster. *B*: Cx43 protein levels estimated by Western analysis. Amount of Cx43 was normalized to the value of GAPDH protein. *$P < 0.01$ vs. 6 wk of the same strain: #$P < 0.01$ vs. age-matched golden hamster. *C*: Cx45 protein levels estimated by Western analysis. The amount of Cx45 was normalized to the value of GAPDH protein. Open bars: golden hamsters; closed bars: UM-X7.1 hamsters. All data were normalized to the value of an age 6-wk golden hamster, which was set to a value 1.

Figure 6*B* shows representative changes in the action potential configuration. Figure 6*A*, *top*, shows color maps of $APD_{90}$ during constant stimulation from the apex. The $APD_{90}$ values in the entire mapping area are displayed as color gradients with the shortest $APD_{90}$ colored red and the longest colored blue. Figure 6*A*, *bottom*, shows superimposed optical action potential signals recorded from 16 sites covering a 6 × 6-mm square. In golden hamsters at both ages 10 and 20 wk, the $APD_{90}$ maps were homogeneously colored red with a minimal dispersion of $APD_{90}$, and there were no appreciable age-dependent changes (Fig. 6*B*; Table 2). In UM-X7.1 hamsters, the averaged $APD_{90}$ was unaffected at age 10 wk, whereas it was prolonged at 20 wk compared with golden hamsters. The dispersion of $APD_{90}$ in UM-X7.1 was significantly larger than golden hamsters even at age 10 wk, reflected by a mixture of red and blue (Fig. 6*B*). The APD dispersion in UM-X7.1 was more pronounced at age 20 wk (Table 2).

Induction of VT/VF was attempted by a premature stimulation protocol. After 19 basic rapid stimulations (S1-S1 150 ms), a single premature stimulus (S2) was applied with progressive shortening of the S1-S2 interval. In golden hamsters ($n$ = 10 and 11 at ages 10 and 20 wk, respectively), no arrhythmias were induced. In UM-X7.1, in contrast, VT or VF was induced in 3 of 11 hamsters at age 10 wk (27%, $P = 0.075$ vs. golden at age 10 wk) and 6 of 6 hamsters at age 20 wk (100%, $P < 0.0001$ vs. golden at age 20 wk; $P < 0.005$ vs. UM-X7.1 at age 10 wk; Table 3). Optical images of VT/VF episodes lasting >5 s were recorded in four UM-X7.1 hearts at age 20 wk. Representative data are shown in Fig. 7. Polymorphic VT (PVT) was induced in one UM-X7.1 hamster at age 20 wk, whereas no arrhythmias were induced in a same age golden hamster (Fig. 7*A*). Figure 7*B* shows six sequential phase maps at the initiation of PVT (see Supplemental Movie 3). A PS of counterclockwise rotation (white circle) appeared in the upper middle region of the LV (133 ms after S2) and moved back and forth in the middle region (208–258 ms). A second PS of clockwise rotation (black circle) appeared in the upper right region at 258 ms and stayed there until the end of the data sampling (500 ms) with minimal meandering. A third PS of counterclockwise rotation coming from the upper left margin (294 ms) collided with the first PS, resulting in their dissipation (mutual annihilation) at 337 ms. A fourth PS of clockwise rotation and a fifth PS of counterclockwise rotation appeared near the apex at 389 and 448 ms, respectively, constructing a figure eight reentry circuit. The distance between the two PSs initially increased and then decreased, culminating in mutual annihilation (461 ms). In addition to these multiple PSs, multiple wavebreaks of incomplete rotation appeared frequently during the PVT episode (black arrowheads at 208 and 294 ms). Complex movements of the five PSs are illustrated in Fig. 7*C*. Figure 7*D* shows the change in PS number during the PVT episode (from 100–500 ms after S2). The average number of

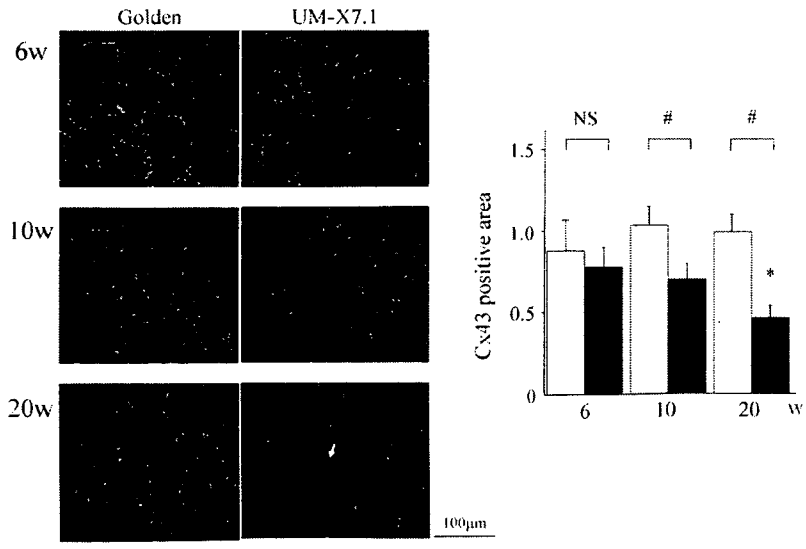


Fig. 4. Confocal images of Cx43 immunolabeling. *Left*: representative confocal images of Cx43 immunolabeling in golden and UM-X7.1 hamster LV. *Right*: proportion of total cell area occupied by the Cx43 immunoreactive signal ($n$ = 5 in each group). Total Cx43 immunolabeling decreased especially at cell termini (arrow). *$P < 0.01$ vs. 6 wk of the same strain; #$P <$ 0.01 vs. age-matched golden hamster.

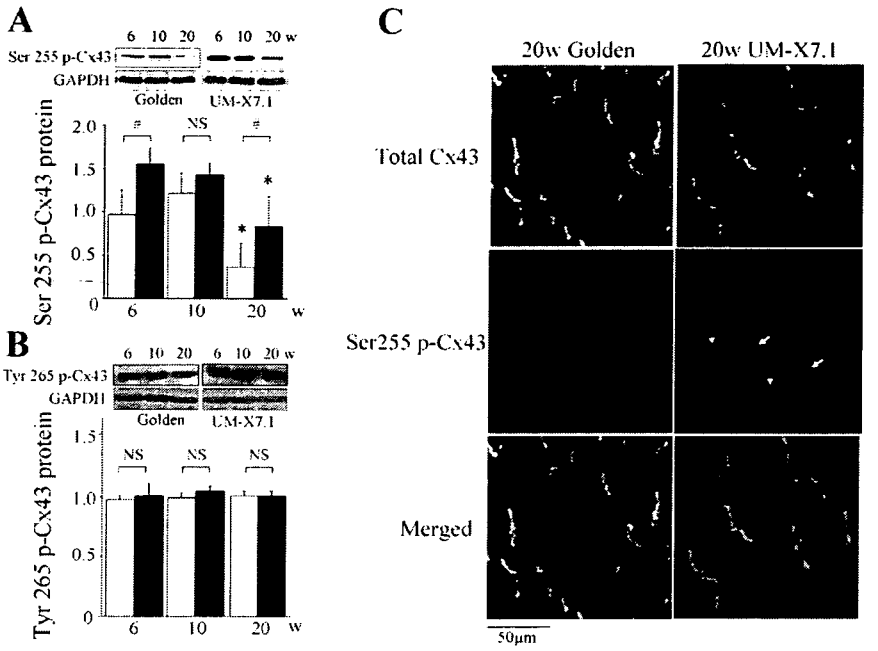


Fig. 5. Phosphorylated Cx43 expression ($n$ = 5 in each group). *A*: Ser255-phosphorylated Cx43 expression. Amount of Ser255-phosphorylated Cx43 was normalized to the value of GAPDH protein. *$P$ < 0.01 vs. 6 wk of the same strain: #$P$ < 0.01 vs. age-matched golden hamster. *B*: Tyr265-phosphorylated Cx43 expression. Amount of Tyr265-phosphorylated Cx43 was normalized to the value of GAPDH protein. Open bars: golden hamsters; closed bars: UM-X7.1 hamsters. All data were normalized to the value of an age 6-wk golden hamster, which was set to a value 1. *C*: representative double staining for total Cx43 (green), Ser255-phosphorylated Cx43 (red), and merged (yellow). In age 20-wk golden hamster LV, total Cx43 staining mainly exists at the cell termini. In age 20-wk UM-X7.1 hamster, total Cx43 staining at cell termini was decreased, and Ser255-phosphorylated Cx43 immunolabeling increased at cell termini (arrow) and in the cytoplasmic area (arrowhead). Arrow indicates Ser255-phosphorylated Cx43.

PSs during the 400 ms was 1.92. Qualitatively similar complex activation patterns with multiple PSs and wavebreaks were observed in phase maps of the remaining VT/VF episodes.

*Intercellular electrical coupling.* Application of subthreshold chathodal unipolar stimuli resulted in instantaneous membrane depolarization spatially localized in the vicinity of the stimulus electrode (Fig. 8*A*, *left*, and *B*), whereas suprathreshold stimuli induced propagating action potentials (Fig. 8*A*, *right*). The amplitude of membrane depolarization in response to subthreshold stimuli was decreased in space almost exponentially with increasing distances from the site of stimulation (Fig. 8, *C* and *D*). The λ estimated from the spatial decay of the subthreshold membrane depolarization varied along and across the myocardial fiber orientation ($\lambda_L$ and $\lambda_T$, respectively, in Fig. 8*D*), reflecting a normal uniform anisotropic architecture of ventricular myocardium. Representative values of $\lambda_L$ and $\lambda_T$ obtained from a golden hamster at age 20 wk (Fig. 8*D*) were comparable to those reported for adult guinea pig ventricular myocardium (3). The difference between control and UM-X7.1 hamsters was analyzed only for $\lambda_T$, because precise evaluation of $\lambda_L$ was often hampered by small hyperpolarization of membrane potential 1- to 2-mm distant in the direction along the fiber orientation from the stimulation site when relatively large subthreshold stimuli were applied. This may be the result of virtual

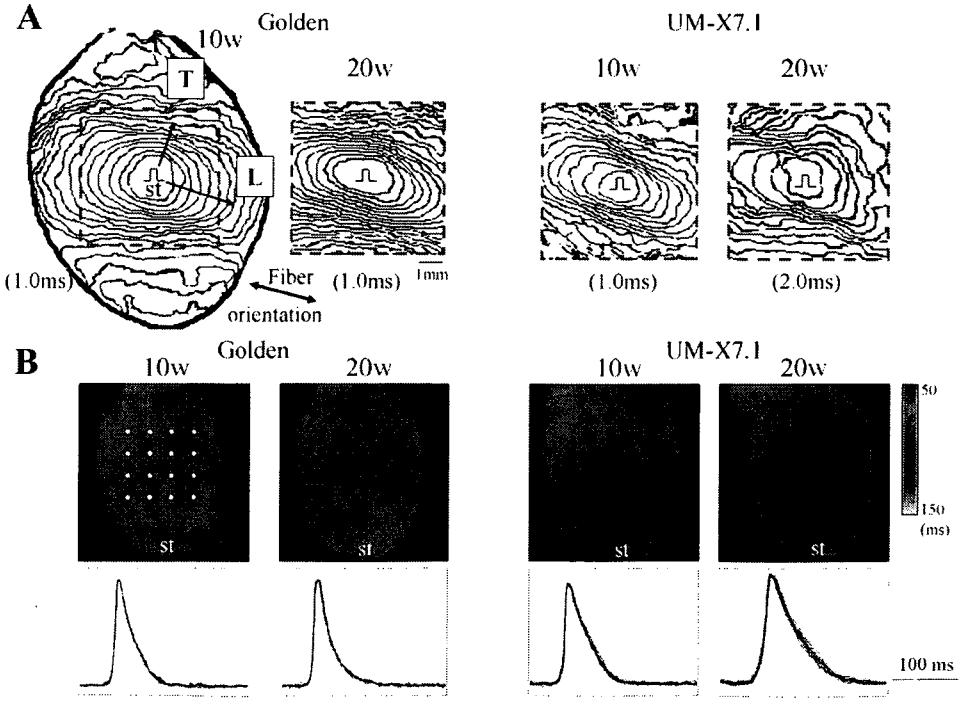


Fig. 6. Conduction properties and action potential configurations in golden and UM-X7.1 hamsters at ages 10 and 20 wk. *A*: isochrone maps of activation during constant stimulation [basic cycle length (BCL) = 200 ms]; 1.0-ms intervals for golden at ages 10 wk and 20 wk and UM-X7.1 at age 10 wk and 2.0-ms intervals for UM-X7.1 at age 20 wk. A dotted square (6 × 6 mm) surrounds the area for measurements of conduction velocity. L, longitudinal direction; T, transverse direction. Bidirectional arrow indicates the subepicardial myocardial fiber orientation confirmed in the histological section (hematoxylin & eosin) cut parallel to the epicardial surface. *B*: action potential duration at 90% repolarization ($APD_{90}$) and its distribution on the anterior surface of LV. *Top*: maps of $APD_{90}$ in the recording area are displayed as color gradients in 1-ms steps ranging from red (shortest) to blue (longest). Records were obtained during constant stimulation (BCL = 200 ms) from the apex (st). *Bottom*: superimposed action potential signals recorded at 16 sites (white dots on *top*).

Table 2. *Conduction properties and action potential configurations*

| | Golden | | UM-X7.1 | |
|---|---|---|---|---|
| | 10 wk | 20 wk | 10 wk | 20 wk |
| $CV_L$, cm/s | 43.9±0.6 | 43.6±1.1 | 41.8±1.6 | 28.2±1.1†§ |
| $CV_T$, cm/s | 17.4±2.3 | 17.4±1.5 | 18.0±1.8 | 10.5±1.1†§ |
| $CV_L/CV_T$ | 2.6±0.5 | 2.5±0.2 | 2.2±0.3 | 2.7±0.2 |
| $CC_L$ | 0.99±0.01 | 0.99±0.01 | 0.99±0.00 | 0.93±0.01†§ |
| $CC_T$ | 0.98±0.00 | 0.98±0.01 | 0.99±0.01 | 0.86±0.02†§ |
| $APD_{90}$, ms | 84±4 | 78±6 | 88±6 | 131±9†§ |
| APDD, ms | 11.0±2.0 | 10.0±5.3 | 19.7±5.5‡ | 28.0±2.6*§ |

Values are means ± SD ($n$ = 5 in each group). $CV_L$, conduction velocity in the longitudinal direction; $CV_T$, conduction velocity in the transverse direction; $CV_L/CV_T$, anisotropic ratio of conduction velocity; $CC_L$, correlation coefficient between activation time and distances for the measurement of $CV_L$; $CC_T$, correlation coefficient between activation time and distances for the measurement of $CV_T$; $APD_{90}$, action potential duration at 90% repolarization (average of values at 16 sites); APDD, $APD_{90}$ dispersion among 16 sites. Parameters were measured under constant stimulation at a cycle length of 200 ms. *$P < 0.05$, †$P < 0.01$ vs. 10 wk of the same strain; ‡$P < 0.05$, §$P < 0.01$ vs. golden hamster.

electrode polarization (3). There was no significant difference in $\lambda_T$ between UM-X7.1 and golden hamsters at age 10 wk. At age 20 wk, the average $\lambda_T$ in UM-X7.1 was significantly less than that in golden hamsters (Fig. 8*E*, $n$ = 4 in each group).

## DISCUSSION

The novel finding of this study is that UM-X7.1 cardiomyopathic hamsters at a compensated stage of heart failure show a ~55% reduction in the amount of Cx43 protein and abnormal phosphorylation in the ventricular myocardium in addition to mild interstitial fibrosis. These changes were associated with a decrease in cardiac $\lambda$, an inhibition of conduction, an increased dispersion of repolarization, and an enhanced propensity to VT/VF resulting from multiple reentrant circuits with complex meandering. In UM-X7.1 hamsters, quantitative and qualitative alterations of Cx43 in concert with interstitial fibrosis may therefore create serious arrhythmogenic substrates through an inhibition of cell-to-cell coupling.

*Downregulation of Cx43 in failing hearts.* It is now well recognized that conduction disturbance in the failing heart is attributed at least in part to disturbances of gap junction organization. The most consistently observed alteration in ventricular Cx expression involves downregulation of Cx43 in patients with end-stage heart failure due to idiopathic dilated cardiomyopathy or ischemic heart disease (31). Downregulation of Cx43 was also demonstrated in several animal models. In dog hearts with pacing-induced heart failure, Poelzing and Rosenbaum (28) reported that a substantial reduction of immunoreactive Cx43 (by 40% in average) was accompanied by a significant reduction in intercellular coupling and CV in association with an enhancement of transmural dispersion of APD. In a study using similar dog model of heart failure, Akar et al. (5) showed not only a quantitative reduction of Cx43 protein expression but also redistribution of Cx43 from the intercalated disk region to lateral cell borders and relative increase of hypophosphorylated fraction of Cx43. In a transgenic mouse model of juvenile dilated cardiomyopathy, Hall et al. (16) showed that a reduction of Cx43 expression and conduction defect become apparent long before development of severe congestive heart failure. The present study using the cardiomyopathic hamster UM-X7.1 is in line with their study in terms of Cx43 downregulation during the development of heart failure.

In our cardiomyopathic hamster model, although immunofluorescence data revealed significant decrease in Cx43 at age 10 wk (hypertrophic stage; Fig. 4), the total content of Cx43 estimated by Western blotting showed no significant Cx43 reduction compared with golden hamsters at the same age (Fig. 3*B*). A possible explanation for this inconsistency may be translocation of Cx43 from the surface membrane to the cytosol, which is detected by Western blot.

In failing hearts, activation of several neurohumoral factors (e.g., rennin-angiotensin- aldosterone system, cytokines, and cathechlamines) could affect synthesis, assembly, disassembly, degradation, and phosphorylation of connexins. The downregulation and altered phosphorylation of Cx43 in UM-X7.1 hamster hearts could be reversed by inhibitors of such neurohumoral factors. These issues were not studied in the present experiments. Phosphorylation of Cx43 on Ser255 by $p34^{cdc2}$ kinase in Rat1 cells was shown to promote endocytosis and degradation (22). It seems reasonable to speculate that translocation and degradation of Cx43 in cardiac cells might be the result of phosphorylation of specific residues.

*Alterations in Cx43 as arrhythmogenic substrates.* The relationship between the quantitative changes in Cx43 expression and conduction properties of the cardiac impulse has been studied in a variety of genetically engineered mouse models. Data on conduction properties in heterozygous knockout (KO) mice (~50% reduction of Cx43), which develop normally and have normal lifespan, are contradictory; some investigators reported 23~44% conduction slowing (12, 14), whereas others detected no significant conduction abnormalities (24). Gutstein et al. (15) demonstrated in cardiac-restricted Cx43 KO mice that a marked reduction of Cx43 (by 95%) resulted in a significant reduction in CV (by 42–55%) and a high incidence of spontaneous lethal ventricular tachyarrhythmias. The same group studied the quantitative relationship of Cx43 downregulation, conduction disturbance, and ventricular arrhythmia inducibility by using a subline of Cx43 KO mice with progressively decreasing levels of Cx43 at older ages (9). The results revealed that an ~80% reduction of Cx43 is required for the genesis of serious arrhymogenic conduction disturbance.

In the present study with the use of UM-X7.1 hamsters, a moderate reduction of Cx43 (by 55% at age 20 wk) was

Table 3. *VT/VF induction by premature stimulation*

| | Total Animal Number | Nonsustained VT (3 beats ~ 5 s) | Sustained VT/VF (>5 s) | Total VT/VF |
|---|---|---|---|---|
| Golden | | | | |
| 10 wk | 10 | 0 (0%) | 0 (0%) | 0 (0%) |
| 20 wk | 11 | 0 (0%) | 0 (0%) | 0 (0%) |
| UM-X7.1 | | | | |
| 10 wk | 11 | 2 (18%) | 1 (9%) | 3 (27%) |
| 20 wk | 6 | 1 (17%) | 5 (83%)*‡ | 6 (100%)*† |

Values are numbers and proportions (in parenthesis) of hamsters showing VT or VF episodes. To induce VT or VF, a single premature stimulus (S2) was applied after rapid conditioning stimuli (S1 × 19, S1-S1 = 150 ms) with progressive shortening of S1-S2 coupling interval. VT/VF episodes were divided into nonsustained (3 beats ~ 5 s) and sustained (>5 s) types. *$P <$ 0.0001 vs. age-matched golden; †$P < 0.005$ vs. UM-X7.1 at age 10 wk.

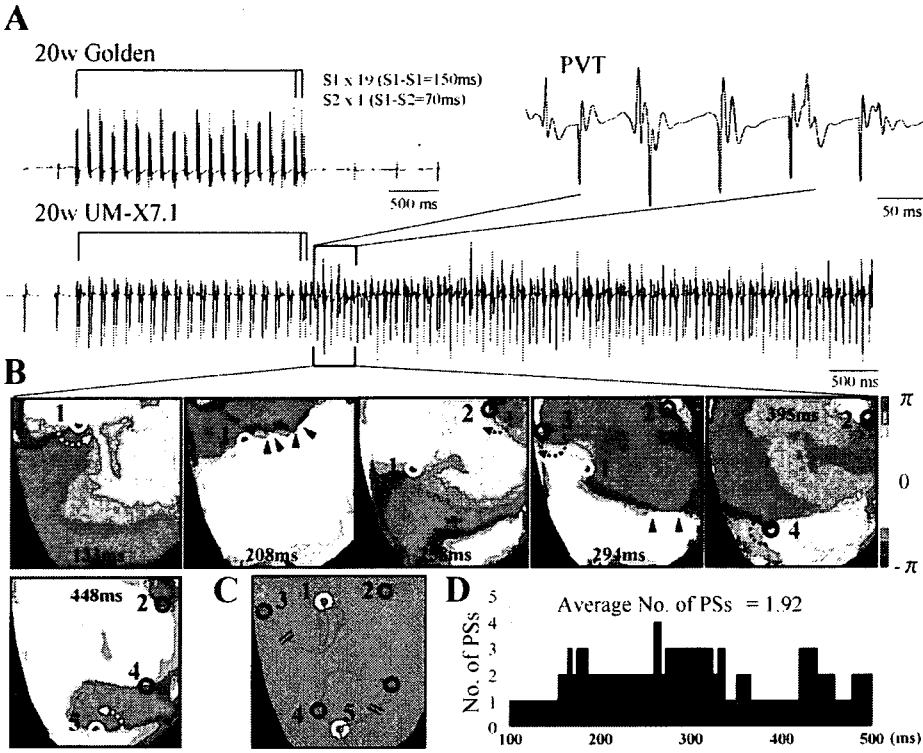


Fig. 7. Polymorphic ventricular tachycardia (PVT) induced by premature stimulation. *A*: tracings of bipolar electrograms during and after premature stimulation. *Top*: a record from a golden hamster at age 20 wk. No arrhythmias were induced by premature stimulation (S2) after 19 rapid conditioning stimuli (S1-S1 = 150 ms) with the shortest coupling interval of ventricular capture (S1-S2 = 70 ms). *Bottom*: a record from a UM-X7.1 hamster at age 20 wk. PVT was induced by the same premature stimulation protocol. Electrograms during an initial period of PVT (100–500 ms after S2) were expanded (*right top*) to reveal the polymorphic configuration. Optical action potential signals in the whole mapped area during the initial period of PVT were analyzed by the phase mapping method. *B*: 6 snapshots of phase maps (133–448 ms). Phase singularities (PSs) are indicated by circles (black for clockwise and white for counterclockwise rotation). Black arrowheads indicate wavebreaks with incomplete rotation. *C*: trajectories of 5 PSs are indicated by red lines. *D*: number of PSs over 400 ms during the VT episode.

associated with significant reduction of CV (by 35~40%), an increased dispersion of ventricular repolarization, and a high susceptibility to VT/VF induction. This suggests some additional factors to compromise the normal uniform conduction in the cardiomyopathic hamster.

An age-dependent progression of fibrosis (from ages ~10 wk) may be most important among these factors. According to the cable theory, the CV is inversely proportional to the square root of tissue resistivity, which is composed of intracellular ($R_i$) and extracellular ($R_o$) resistances (21). Interstitial fibrosis is expected to cause an increase of $R_o$ and if it is combined with an increase of $R_i$ resulting from Cx43 downregulation, the net effect to compromise conduction would be much greater than the increase of $R_i$ alone. Our experiments to measure spatial decay of electrotonic depolarization in response to subthreshold stimuli showed that effective λ, which is also inversely proportional to the square root of tissue resistivity ($R_i + R_o$) in the cable theory, was in fact significantly less in UM-X7.1 at age 20 wk (by 32%) compared with golden hamsters at the same age. Spach et al. (32) have demonstrated in their simulation study that cellular scaling (cell size) plays an important role in determining anisotropic conduction properties by affecting the cell-to-cell delay of activation and the maximum upstroke velocity. In UM-X7.1 hamsters at age 10 wk, the

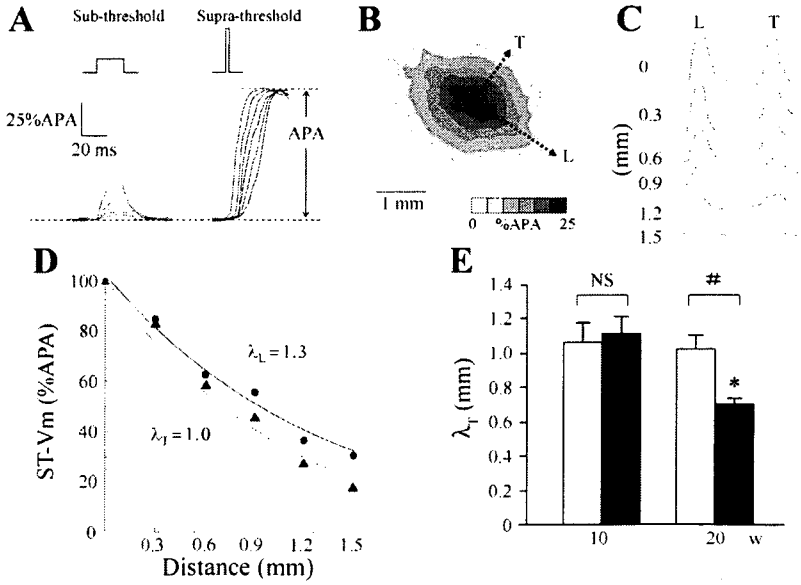


Fig. 8. Cardiac space constant (λ) assessed by spatial decline of electrotonic membrane depolarization. *A*: optical recording of transmembrane potential ($V_m$) in response to stimuli at intensities below (*left*) and above (*right*) the diastolic threshold from 6 sites 0–1.5 mm away from the stimulus electrode. *Top*: schematic representation of the stimulus pulse; *bottom*: superimposed traces of $V_m$. APA, amplitude of action potential induced by suprathreshold stimuli. Dotted line indicates the resting $V_m$ level. *B*: spatial distribution of subthreshold (ST) $V_m$ changes (ST-$V_m$) surrounding the site of ST stimulation shown as isopotential plot. *C*: ST-$V_m$ shown for sites 0–1.5 mm from the stimulating electrode along the longitudinal and transverse axes of propagation. *D*: decay of ST-$V_m$ in space plotted along (circles) and across (triangles) fiber orientation. λ was calculated from the exponential decay constant in each direction. *E*: comparison of $\lambda_T$ between golden (control: open bars) and UM-X7.1 (closed bars) hamsters at ages 10 and 20 wk ($n$ = 4 at each age). At age 20 wk, $\lambda_T$ in UM-X7.1 was significantly less (by 32%) than that in golden hamsters. *$P < 0.01$ vs. 10 wk of the same strain; #$P < 0.01$ vs. age-matched golden hamster.

anisotropic conduction properties were unaffected despite of significant increase in cell size. This apparent discrepancy might be due to a relatively small cell hypertrophy (an increase of cell width by ~25%) in the UM-X7.1 hamster compared with the simulation by Spach et al. (~4-fold increase in cell surface area). Concomitant moderate increase (~5%) of connective tissue (fibrosis) in the UM-X7.1 hamster might have different effects on the anisotropic conduction properties to make the issue more complex.

The second factor to be considered is phosphorylation of gap junction proteins affecting the channel conductance, trafficking, and/or the assembly or disassembly (22, 30). Rapid dephosphorylation and translocation of Cx43 from the intercalated disk region have been reported in rat hearts subjected to acute ischemia (7). Dephosphorylation of Cx43 and inhibition of intercellular communincation have also been reported in animal models of nonischemic heart failure (1, 5). On the other hand, the phosphorylation of specific serine sites (e.g., Ser368 by PKC and Ser255, Ser279, and Ser282 by MAPK) or a tyrosine site (e.g., Tyr265 by Src) in Cx43 was reported to cause a rapid attenuation of gap junction channel communication (22). Toyofuku et al. (34) demonstrated in BIO14.6 cardiomyopathic hamster hearts that the level of Tyr265-phosphorylated Cx43 was increased at the advanced stage of heart failure and that the change was accompanied by an increase in c-Src activity and a reduction in gap junctional communication.

In the present study, despite the reduction in total Cx43 expression, the expression of Ser255-phosphorylated Cx43 was significantly increased in UM-X7.1 at age 20 wk compared with golden hamsters at the same age. In contrast, there was no significant difference in the expression level of Tyr265-phosphorylated Cx43 between the two animal groups. Interestingly, Ser255-phosphorylated Cx43 was upregulated not only at the intercalated disc region but also in the cytosolic area. Based on these observations, it seems reasonable to speculate that relative increase of dysfunctional or nonfunctional Ser255-phosphorylated Cx43 gap junctions in UM-X7.1 may contribute as well to the inhibition of cell-to-cell electrical coupling in the heart.

The present results showed that there was a marked age-dependent reduction of Ser255-phosphorylated Cx43 in golden hamsters and that the age-dependent change was attenuated in UM-X7.1 The pathophysiological meaning of this observation remains unclear, and further experimental studies will be required to elucidate the issue.

The third factor to be addressed is potential changes in other Cx members. Yamada et al. (41) reported upregulation of Cx45 in conjunction with downregulation of Cx43 in the end stage of human failing ventricles. In the present study using UM-X7.1 hamsters, there was no significant difference in the level of Cx45 expression between the cardiomyaopathic and control hamsters at ages 6~20 wk. This result is in line with the study using BIO14.6 cardiomyopathic hamster hearts (34).

### *Study Limitations*

There are several limitations in the present study. First, we estimated electrical cell coupling by measuring overall tissue resistivity. With the use of a high-resolution optical mapping system, spatial decay of transmembrane potential in response to subthreshold depolarizing stimuli was measured, and the $\lambda$ was determined by fitting of the data with a single exponential function according to the method originally described by Akar et al. (3). This is not a direct measure of cell-to-cell coupling, since the tissue resistivity is composed of both $R_i$ and $R_o$ in the cable theory and does not allow distinction between the two parameters. A better direct method to quantify loss of coupling might be to look at individual cell pairs using either current or dye injection. It was, however, practically difficult to isolate ventricular cell pairs, which are suitable for the measurements, from UM-X7.1 hamsters at age 20 wk by enzymatic digestion, because of a plenty of connective tissues and more fragile cell membranes in the pathological condition. In addition, mammalian cardiac tissue is best modeled by bidomain equations with unequal anisotropic ratios of intracellular and extracellular domains rather than a simplified one-dimensional cable equation (21). According to the two or three-dimensional bidomain model, membrane depolarization during unipolar current injection does not decay as a simple exponential function from a point of current injection (21). In optical measurement experiments using Langendorff-perfused guinea pig hearts, however, Akar et al. (3) have demonstrated that there is a close linear relationship between $\lambda$ and the CV at different angles with respect to the fiber orientation and that pharmacological intercellular uncoupling decreases $\lambda$ and the CV in parallel. These observations support the feasibility of $\lambda$ as a useful approximate index of cardiac cell coupling.

Second, we did not investigate remodeling of other ion channels, including the sarcolemmal $Na^+$, $Ca^{2+}$, and $K^+$ channels, which are responsible for depolarization and repolarization of action potentials. Altered expression and function of these ion channels in UM-X7.1 hamsters could contribute to the conduction disturbance and increased dispersion of repolarization in favor of serious reentrant ventricular arrhythmias.

Third, we could not get spontaneous monitoring ECG records of lethal ventricular arrhythmias (PVT/VF) resulting in sudden death in the UM-X7.1 hamsters. Hano et al. (17) reported a high propensity for ventricular arrhythmias in cardiomyopathic hamsters with no signs of heart failure.

Fourth, we could not measure the transmural heterogeneities of cellular repolarization and their potential role in heart failure-related arrhythmias in our mapping system with small animal models. Transmural electrophysiological heterogeneities are known to be an important substrate of arrhythmogenesis in heart failure (4). Finally, our findings are certainly of relevance to hamster models but not necessarily of human idiopathic cardiomyopathy condition specifically.

### ACKNOWLEDGMENTS

This study was supported by in part by a grant-in-aid for scientific research in Japan (C17590738 and C19590818) from the Ministry of Education, Japan.

### REFERENCES

1. **Ai X, Pogwizd SM.** Connexin 43 downregulation and dephosphorylation in nonischemic heart failure is associated with enhanced colocalized protein phosphatase type 2A. *Circ Res* 96: 54–63, 2005.
2. **Amino M, Yamazaki M, Nakagawa H, Honjo H, Okuno Y, Yoshioka K, Tanabe T, Yasui K, Lee JK, Horiba M, Kamiya K, Kodama I.** Combined effects of nifekalant and lidocaine on the spiral-type re-entry in a perfused 2-dimensional layer of rabbit ventricular myocardium. *Circ J* 69: 576–584, 2005.
3. **Akar FG, Roth BJ, Rosenbaum DS.** Optical measurement of cell-to-cell coupling in intact heart using subthreshold electrical stimulation. *Am J Physiol Heart Circ Physiol* 281: H533–H542, 2001.

4. **Akar FG, Rosenbaum DS.** Transmural electrophysiological heterogeneities underlying arrhythmogenesis in heart failure. *Circ Res* 93: 638–645, 2003.
5. **Akar FG, Spragg DD, Tunin RS, Kass DA, Tomaselli GF.** Mechanisms underlying conduction slowing and arrhythmogenesis in nonischemic dilated cardiomyopathy. *Circ Res* 95: 717–725, 2004.
6. **Bansch D, Antz M, Boczor S, Volkmer M, Tebbenjohanns J, Seidel K, Block M, Gietzen F, Berger J, Kuck KH.** Primary prevention of sudden cardiac death in idiopathic dilated cardiomyopathy: the cardiomyopathy trial. *Circulation* 105: 1453–1458, 2002.
7. **Beardslee MA, Lerner DL, Tadros PN, Laing JG, Beyer EC, Yamada KA, Kléber AG, Schuessler RB, Saffitz JE.** Dephosphorylation and intracellular redistribution of ventricular connexin43 during electrical uncoupling induced by ischemia. *Circ Res* 87: 656–662, 2000.
8. **Beauchamp P, Choby C, Desplantez T, de Peyer K, Green K, Yamada KA, Weingart R, Saffitz JE, Kléber AG.** Electrical propagation in synthetic ventricular myocyte strands from germline connexin43 knockout mice. *Circ Res* 95: 170–178, 2004.
9. **Danik SB, Liu F, Zhang J, Suk HJ, Morley GE, Fishman GI, Gutstein DE.** Modulation of cardiac gap junction expression and arrhythmic susceptibility. *Circ Res* 95: 1035–1041, 2004.
10. **Deroubaix E, Thuringer D, Coulombe A, Mercadier JJ, Coraboeuf E.** Dilation and action potential lengthening in cardiomyopathic Syrian hamster heart. *Basic Res Cardiol* 94: 274–283, 1994.
11. **Dhein S, Krusemann K, Schaefer T.** Effects of gap junction uncoupler palmitoleic acid on the activation and repolarization wavefronts in isolated rabbit hearts. *Br J Pharmacol* 128: 1375–1384, 1999.
12. **Eloff BC, Lerner DL, Yamada KA, Schuessler RB, Saffitz JE, Rosenbaum DS.** High resolution optical mapping reveals conduction slowing in connexin43 deficient mice. *Cardiovasc Res* 51: 681–690, 2001.
13. **Gray RA, Pertsov AM, Jalife J.** Spatial and temporal organization during cardiac fibrillation. *Nature* 392: 75–78, 1998.
14. **Guerrero PA, Schuessler RB, Davis LM, Beyer EC, Johnson CM, Yamada KA, Saffitz JE.** Slow ventricular conduction in mice heterozygous for a connexin43 null mutation. *J Clin Invest* 99: 1991–1998, 1997.
15. **Gutstein DE, Morley GE, Tamaddon H, Vaidya D, Schneider MD, Chen J, Chien KR, Stuhlmann H, Fishman GI.** Conduction slowing and sudden arrhythmic death in mice with cardiac-restricted inactivation of connexin43. *Circ Res* 88: 333–339, 2001.
16. **Hall DG, Morley GE, Vaidya D, Ard M, Kimball TR, Witt SA, Colbert MC.** Early onset heart failure in transgenic mice with dilated cardiomyopathy. *Pediatr Res* 48: 36–42, 2000.
17. **Hano O, Mitsuoka T, Matsumoto Y, Ahmed R, Hirata M, Hirata T, Mori M, Yano K, Hashiba K.** Arrhythmogenic properties of the ventricular myocardium in cardiomyopathic Syrian hamster, BIO 14.6 strain. *Cardiovasc Res* 25: 49–57, 1991.
18. **Inoue N, Ohkusa T, Nao T, Lee Matsumoto T JK, Hisamatsu Y, Satoh T, Yano M, Yasui K, Kodama I, Matsuzaki M.** Rapid electrical stimulation of contraction modulates gap-junction protein in neonatal rat cultured cardiomyocytes: Involvement of mitogen-activated protein kinases and effects of angiotensin II-receptor antagonist. *J Am Coll Cardiol* 44: 914–922, 2004.
19. **Jongsma HJ, Wilders R.** Gap junctions in cardiovascular disease. *Circ Res* 86: 1193–1197, 2000.
20. **Kaprielian RR, Gunning M, Dupont E, Sheppard MN, Rothery SM, Underwood R, Pennell DJ, Fox K, Pepper J, Poole-Wilson PA, Severs NJ.** Downregulation of immunodetectable connexin43 and decreased gap junction size in the pathogenesis of chronic hibernation in the human left ventricle. *Circulation* 97: 651–660, 1998.
21. **Kléber AG, Janse MJ, Fast VG.** Normal and abnormal conduction in the heart. In: *Handbook of Physiology Section 2, The Cardiovascular System*, edited by Page E, Fozard HA, and Solaro RJ. New York: Oxford University Press, p. 455–530, 2001.
22. **Lampe PD, Lau AF.** Regulation of gap junctions by phosphorylation of connexins. *Arch Biochem Biophys* 284: 205–215, 2000.
23. **Lee MH, Lin SF, Ohara T, Omichi C, Okuyama Y, Chudin E, Garfinkel A, Weiss JN, Karagueuzian HS, Chen PS.** Effects of diacetyl monoxime and cytochalasin D on ventricular fibrillation in swine right ventricles. *Am J Physiol Heart Circ Physiol* 280: H2689–H2696, 2001.
24. **Morley GE, Vaidya D, Samie FH, Lo C, Delmar M, Jalife J.** Characterization of conduction in the ventricles of normal and heterozygous Cx43 knockout mice using optical mapping. *J Cardiovasc Electrophysiol* 10: 1361–1375, 1999.
25. **Mullis K, Faloona F, Scharf S, Saiki R, Horn G, Erlich H.** Specific enzymatic amplification of DNA in vitro: the polymerase chain reaction. *Cold Spring Harb Symp Quant Biol* 51: 263–273, 1986.
26. **Ohkusa T, Ueyama T, Yamada J, Yano M, Fujumura Y, Esato K, Matsuzaki M.** Alterations in cardiac sarcoplasmic reticulum $Ca^{2+}$ regulatory proteins in the atrial tissue of patients with chronic atrial fibrillation. *J Am Coll Cardiol* 34: 255–263, 1999.
27. **Peters NS, Coromilas J, Severs NJ, Wit AL.** Disturbed connexin43 gap junction distribution correlates with the location of reentrant circuits in the epicardial border zone of healing canine infarcts that cause ventricular tachycardia. *Circulation* 95: 988–996, 1997.
28. **Poelzing S, Rosenbaum DS.** Altered connexin43 expression produces arrhythmia substrate in heart failure. *Am J Physiol Heart Circ Physiol* 287: H1762–H1770, 2004.
29. **van Rijen HV, Eckardt D, Degen J, Theis M, Ott T, Willecke K, Jongsma HJ, Opthof T, de Bakker JM.** Slow conduction and enhanced anisotropy increase the propensity for ventricular tachyarrhythmias in adult mice with induced deletion of connexin43. *Circulation* 109:1048–1055, 2004.
30. **Saffitz JE, Laing JG, Yamada KA.** Connexin expression and turnover: implications for cardiac excitability. *Circ Res* 86: 723–728, 2000.
31. **Severs NJ, Coppen SR, Dupont E, Yeh HI, Ko YS, Matsushita T.** Gap junction alterations in human cardiac disease. *Cardiovasc Res* 62: 368–377, 2004.
32. **Spach MS, Heidlage JF, Dolber PC, Barr RC.** Elelctrophysiological effects of remodeling cardiac gap junctions and cell size. Experimental and model studies of normal cardiac growth. *Circ Res* 86: 302–311, 2000.
33. **Takahashi T, Allen PD, Izumo S.** Expression of A-, B-, and C-type natriuretic peptide gene in failing and developing human ventricles: correlation with expression of the $Ca^{2+}$-ATPase gene. *Circ Res* 71: 9–17, 1992.
34. **Toyofuku T, Yabuki M, Otsu K, Kuzuya T, Tada M, Hori M.** Functional role of c-Src in gap junctions of the cardiomyopathic heart. *Circ Res* 85: 672–681, 1999.
35. **Tso JY, Sun XH, Kao TH, Reece KS, Wu R.** Isolation and characterization of rat and human glyceraldehyde-3-phosphate dehydrogenase cDNAs: genomic complexity and molecular evolution of the gene. *Nucleic Acids Res* 13: 2485–2502, 1985.
36. **Ueyama T, Ohkusa T, Hisamatsu Y, Nakamura Y, Yamamoto T, Yano M, Matsuzaki M.** Alterations in cardiac SR $Ca^{2+}$-release channels during development of heart failure in cardiomyopathic hamsters. *Am J Physiol Heart Circ Physiol* 274: H1–H7, 1998.
37. **Ueyama T, Ohkusa T, Yano M, Matsuzaki M.** Growth hormone preserves cardiac sarcoplasmic reticulum $Ca^{2+}$ release channels (ryanodine receptors) and enhances cardiac function in cardiomyopathic hamsters. *Cardiovasc Res* 40: 64–73, 1998.
38. **Uzzaman M, Honjo H, Takagishi Y, Emdad L, Magee AI, Severs NJ, Kodama I.** Remodeling of gap junctional coupling in hypertrophied right ventricles of rats with monocrotaline-induced pulmonary hypertension. *Circ Res* 86: 871–878, 2000.
39. **Wang X, Gerdes AM.** Chronic pressure overload cardiac hypertrophy and failure in guinea pigs: III. Intercalated disc remodeling. *J Mol Cell Cardiol* 31: 333–343, 1999.
40. **Warn-Cramer BJ, Cottrell GT, Burt JM, Lau AF.** Regulation of connexin-43 gap junctional intercellular communication by mitogen-activated protein kinase. *J Biol Chem* 273: 9188–9196, 1998.
41. **Yamada KA, Rogers JG, Sundset R, Steinberg TH, Saffitz JE.** Up-regulation of connexin45 in heart failure. *J Cardiovasc Electrophysiol* 14: 1205–1212, 2003.
42. **Yamazaki M, Honjo H, Nakagawa H, Ishiguro YS, Okuno Y, Amino M, Sakuma I, Kamiya K, Kodama I.** Mechanisms of destabilization and early termination of spiral wave reentry in the ventricle by a class III antiarrhythmic agent, nifekalant. *Am J Physiol Heart Circ Physiol* 292: H539–H548, 2007.
43. **Yao JA, Hussain W, Patel P, Peters NS, Boyden PA, Wit AL.** Remodeling of gap junctional channel function in epicardial border zone of healing canine infarcts. *Circ Res* 92: 437–443, 2003.
44. **Yao JA, Gutstein DE, Liu F, Fishman GI, Wit AL.** Cell coupling between ventricular myocyte pairs from connexin43-deficient murine hearts. *Circ Res* 93: 736–743, 2003.
45. **Zhuang J, Yamada KA, Saffitz JE, Kléber AG.** Pulsatile stretch remodels cell-to-cell communication in cultured myocytes. *Circ Res* 87: 316–322, 2000.

THE JOURNAL OF BIOLOGICAL CHEMISTRY VOL. 283, NO. 1, pp. 166–174, January 4, 2008

# Regulation of Platelet Dense Granule Secretion by the Ral GTPase-Exocyst Pathway*

Received for publication, June 28, 2007, and in revised form, September 28, 2007 Published, JBC Papers in Press, October 15, 2007, DOI 10.1074/jbc.M705340200

**Mitsunori Kawato[‡], Ryutaro Shirakawa[‡1], Hirokazu Kondo[‡], Tomohito Higashi[‡1], Tomoyuki Ikeda[‡], Katsuya Okawa[§], Shuya Fukai[¶], Osamu Nureki[¶], Toru Kita[‡], and Hisanori Horiuchi[‡2]**

*From the [‡]Department of Cardiovascular Medicine and [§]Frontier Technology Center, Graduate School of Medicine, Kyoto University, Kyoto, 606-8507, Japan, [¶]Department of Bioscience and Biotechnology, Tokyo Institute of Technology, Yokohama, 226-8501, Japan, and Life Science Division, Synchrotron Radiation Research Organization, University of Tokyo, Tokyo, 113-0032, Japan*

Non-hydrolyzable GTP analogues, such as guanosine 5′-(β,γ-imido)triphosphate (GppNHp), induce granule secretion from permeabilized platelets in the absence of increased intracellular $Ca^{2+}$. Here, we show that the GppNHp-induced dense granule secretion from permeabilized platelets occurred concomitantly with the activation of small GTPase Ral. This secretion was inhibited by the addition of GTP-Ral-binding domain (RBD) of Sec5, which is a component of the exocyst complex known to function as a tethering factor at the plasma membrane for vesicles. We generated an antibody against Sec5-RBD, which abolished the interaction between GTP-Ral and the exocyst complex *in vitro*. The addition of this antibody inhibited the GppNHp-induced secretion. These data indicate that Ral mediates the GppNHp-induced dense granule secretion from permeabilized platelets through interaction with its effector, the exocyst complex. Furthermore, GppNHp enhanced the $Ca^{2+}$ sensitivity of dense granule secretion from permeabilized platelets, and this enhancement was inhibited by Sec5-RBD. In intact platelets, the association between Ral and the exocyst complex was induced by thrombin stimulation with a time course similar to that of dense granule secretion and Ral activation. Taken together, our results suggest that the Ral-exocyst pathway participates in the regulation of platelet dense granule secretion by enhancing the $Ca^{2+}$ sensitivity of the secretion.

Platelet activation occurs in response to vascular injury and plays an essential role in thrombus formation and hemostasis. Several agonists, including thrombin, adenosine diphosphate (ADP), and thromboxane $A_2$, can activate platelets at sites of vascular injury (1). The activation of platelets by these agonists involves the elevation of intracellular $Ca^{2+}$ concentration, which leads to cell shape change, granule secretion, and platelet aggregation (1, 2). In activated platelets, however, it has been demonstrated that levels of intracellular $Ca^{2+}$ vary considerably, ranging from 0.2 to 2 μM (3).

Platelets store self-agonists, such as ADP and serotonin, in dense granules (2, 4). Release of these contents plays an important role in further platelet activation and recruitment of circulating platelets to the site of vascular injury. Although an increase in intracellular $Ca^{2+}$ concentration is the trigger for regulated exocytosis in platelets (5, 6), it has long been known that non-hydrolyzable GTP analogues, such as GTPγS[3] and GppNHp, induce granule secretion from permeabilized platelets even at low concentrations of $Ca^{2+}$ (7–11). Non-hydrolyzable GTP analogues have also been shown to shift the $Ca^{2+}$ concentration-response curve for dense granule secretion to the left in electropermeabilized platelets, indicating that GTPγS and GppNHp increase the $Ca^{2+}$ sensitivity of platelet secretion (7). These observations suggest that some GTPases are involved in the process, although the molecular basis remains unclear.

Members of the Ras superfamily of small GTPases are classified into several groups such as Ras subfamily that is implicated in cell proliferation, Rho subfamily involved in cytoskeletal regulation, and Rab subfamily involved in vesicle transport (12, 13). Small GTPases cycle between inactive GDP-bound form and active GTP-bound form that exert their function through specific interaction with effector proteins. The activation process is performed by GDP/GTP exchange reaction that is mediated by GDP/GTP exchange factors. The inactivation process is performed by GTP hydrolysis that is mediated by GTPase-activating proteins.

Ral GTPases are members of the Ras subfamily, consisting of RalA and RalB. Most of the Ral-GDP/GTP exchange factors so far identified, such as Ral-GDP dissociation stimulator, Rgl, and Rlf, are downstream effector molecules of Ras, indicating that Ras controls Ral activation (14, 15). On the other hand, the elevation of intracellular $Ca^{2+}$ levels also induces Ral activation independently of Ras activation (16, 17). Ral GTPases have several effector molecules and exert multiple functions, including

* This work was supported by a research grant-in-aid from the Ministry of Education, Culture, Sports, Science, and Technology of Japan. This study was also supported in part by grants-in-aid from the Takeda Science Foundation and Mitsubishi Pharma Research Foundation. The costs of publication of this article were defrayed in part by the payment of page charges. This article must therefore be hereby marked "*advertisement*" in accordance with 18 U.S.C. Section 1734 solely to indicate this fact.

[1] Recipient of Japan Society for the Promotion of Science (JSPS) Research Fellowship for Young Scientists.

[2] To whom correspondence should be addressed: Dept. of Cardiovascular Medicine, Graduate School of Medicine, Kyoto University, Kyoto, 606-8507, Japan. Tel.: 81-75-751-3778; Fax: 81-75-751-3203; E-mail: horiuchi@kuhp.kyoto-u.ac.jp.

[3] The abbreviations used are: GTPγS, guanosine 5′-(γ-thio)triphosphate; GppNHp, guanosine 5′-(β,γ-imido)triphosphate; GDP, guanosine diphosphate; RBD, Ral-binding domain; GST, glutathione *S*-transferase; SLO, streptolysin-O; MALDI-TOF MS, matrix-assisted laser desorption/ionization time-of-flight mass spectrometry; GLUT4, glucose transporter 4; PKCα, protein kinase Cα.

endocytosis through Ral-binding protein 1 (RalBP1), exocytosis through the exocyst complex, cytoskeletal organization through filamin, and tumorigenesis through yet unknown factors (18, 19). In platelets, both RalA and RalB are abundantly expressed (20, 21) and localized on dense granules (22). Ral is rapidly activated after stimulation with various agonists, and its activation is mediated by an increase in intracellular $Ca^{2+}$ levels (17). However, the function of Ral in platelets remains unclear.

The exocyst complex is composed of eight proteins (Sec3, Sec5, Sec6, Sec8, Sec10, Sec15, Exo70, and Exo84) and has been implicated in tethering of vesicles to specific regions on the plasma membrane in some cell types (23). The exocyst complex is one of the Ral effectors, and Ral binds to Sec5 in a GTP-dependent manner (24–26). Exo84 has also been shown to interact with active Ral (27), and its binding is competitive with Sec5 (28). In budding yeast, the exocyst complex plays an essential role in vesicle transport required for the growth of daughter cells under control of the Rab family small GTPase Sec4p (29, 30). In mammals, the exocyst complex is implicated in the formation of cell polarity by targeting vesicles to the basolateral membrane in epithelial cells (31) through interaction with GTP-Ral (25, 32). Exo70 has been reported to bind the Rho family GTPase TC10 and play a role in the targeting of the glucose transporter 4 (GLUT4) to the plasma membrane in response to insulin stimulation in adipocytes (33, 34).

In this study, we examined the role of Ral GTPase and its effector, the exocyst complex, in platelet dense granule secretion. We demonstrate that Ral regulates the GppNHp-induced dense granule secretion through interaction with the exocyst complex, by showing that the addition of a Ral-binding domain (RBD) of Sec5 or anti-Sec5-RBD antibody inhibits the GppNHp-induced secretion from permeabilized platelets. We further show that GTP-Ral enhanced the $Ca^{2+}$ sensitivity of dense granule secretion from permeabilized platelets and propose that the Ral-exocyst pathway could play a role in dense granule secretion in intact platelets.

## EXPERIMENTAL PROCEDURES

*Constructs, Antibodies, Materials, and Other Methods*—cDNA encoding full-length RalA, RalB, and Sec5-RBD (amino acids 1–120) were cloned from the Marathon-Ready human brain cDNA (Clontech) by PCR. Truncated RalA (amino acids 9–183) was prepared as described (35). Sec5-RBD T11A mutant was produced by PCR mutagenesis. All of the sequences of PCR products were confirmed by sequencing using a 3100 Genetic Analyzer (Applied Biosystems). These cDNAs were subcloned into the prokaryotic expression vector pRSET A (Invitrogen) to produce $His_6$-tagged proteins and pGEX-2T (GE Healthcare) to produce glutathione *S*-transferase (GST) fusion proteins. These $His_6$-tagged and GST fusion proteins were produced in *Escherichia coli* strain BL21 (DE3) and purified according to the manufacturer's instructions. All of the purified recombinant proteins were extensively dialyzed against Buffer A (50 mM Hepes/KOH, pH 7.2, 78 mM KCl, 4 mM $MgCl_2$, 0.2 mM $CaCl_2$, 2 mM EGTA, 1 mM dithiothreitol) and stored at −80 °C until use. Protein concentrations were determined by Bradford's method (Bio-Rad) or from the intensities of the bands on Coomassie Blue-stained SDS-polyacrylamide gels using bovine serum albumin as a standard.

Anti-Sec5-N terminus and anti-Sec8-C terminus polyclonal antibodies were raised in rabbits against the N-terminal peptide of human Sec5 (MSRSRQPPLVTGISPNEGIP, corresponding to amino acids 1–20) and the C-terminal peptide of human Sec8 (EQAAIKQATKDKKITTV, corresponding to amino acids 958–974), respectively. Anti-Sec5-RBD and anti-GST antibodies were raised in rabbits by injecting GST-Sec5-RBD (amino acids 1–120) as an antigen and were affinity-purified from the antiserum. Anti-RalA, anti-Sec8, and anti-protein kinase Cα (PKCα) mouse monoclonal antibodies were purchased from BD Transduction Laboratories. Anti-RalB mouse monoclonal antibody was from Millipore. Anti-$His_6$ mouse monoclonal antibody and rabbit IgG were from Sigma. Horseradish peroxidase-labeled anti-rabbit and anti-mouse IgG polyclonal antibodies were from GE Healthcare; these were used as secondary antibodies for Western blot analysis and visualized by the enhanced chemiluminescence method (GE Healthcare). Streptolysin-O (SLO) was provided by Dr. S. Bhakdi (Mainz University, Mainz, Germany) (36). [$^3$H]Serotonin (20.3 Ci/mmol) was purchased from PerkinElmer Life Sciences. Unless otherwise specified, all of the other chemicals including nucleotides and thrombin were purchased from Sigma.

*Platelet Dense Granule Secretion Assays*—The assay method for the $Ca^{2+}$-induced dense granule secretion using permeabilized platelets was described previously (37–41). The assay for the GppNHp-induced dense granule secretion was developed by modification of this method. Briefly, [$^3$H]serotonin-loaded platelets (~20,000 cpm/assay, $1 \times 10^8$ platelets/assay) were permeabilized with SLO in Buffer A, where the calculated free $Ca^{2+}$ concentration was ~20 nM (42). The permeabilized platelets were incubated with the ATP regeneration system, 100 μM GppNHp, and various tested materials at 4 °C for 15 to 30 min. Then, unless otherwise specified, permeabilized platelets were stimulated at 30 °C for 15 min, and the reaction was stopped by the addition of ice-cold Buffer A (1:4, v/v). Finally, released [$^3$H]serotonin was measured by a liquid scintillation counter (Beckman) after removing platelets by centrifugation. The secretion levels of [$^3$H]serotonin were expressed as percentages of the total [$^3$H]serotonin in the platelets before the final incubation. In the secretion assay using intact platelets, [$^3$H]serotonin-loaded platelets were stimulated with 0.5 unit/ml thrombin at 30 °C for the indicated periods in modified Hepes-Tyrode's buffer (50 mM Hepes/KOH, pH 7.4, 138 mM NaCl, 2.9 mM KCl, 1.8 mM $CaCl_2$, 12 mM $NaHCO_3$, 0.49 mM $MgCl_2$, 5.5 mM glucose), and released [$^3$H]serotonin was measured as described above.

*Assay Analyzing Specific Binding of GST-Sec5-RBD with Active Ral*—GDP- or GppNHp-bound $His_6$-RalA and RalB (10 μg each), prepared as described (40, 43), were incubated with glutathione-Sepharose beads (GE Healthcare) coated with wild-type or mutant GST-Sec5-RBD (20 μg each) at 4 °C for 1 h in Buffer A. After washing the beads, bead-associated $His_6$-Ral proteins were analyzed by immunoblotting with anti-$His_6$ antibody.

*GTP (GppNHp)-Ral Pulldown Assay Using GST-Sec5-RBD*—Platelet samples were lysed (1:4, v/v) in ice-cold Buffer A con-

taining 0.5% Triton X-100 and protease-inhibitor mixture at 4 °C for 5 min followed by centrifugation at 300,000 × *g* for 5 min. Then, the supernatants were incubated with glutathione-Sepharose beads coated with 10 μg of GST-Sec5-RBD at 4 °C for 30 min. After washing the beads, bead-associated Ral proteins were analyzed by immunoblotting with anti-RalA and RalB monoclonal antibodies. Densitometric analysis was performed on the blots using Image J 1.38x software (National Institutes of Health).

*Identification of the Exocyst Complex in Platelets*—Glutathione-Sepharose beads coated with GST alone or GDP- or GTPγS-bound GST-RalA (amino acids 9–183) (30 μg each) were incubated with platelet cytosol (30 mg of proteins) (39, 40) at 4 °C for 1 h followed by washing three times with Buffer A. The bead-associated proteins were analyzed by electrophoresis on an SDS-polyacrylamide gel and staining with Coomassie Blue followed by matrix-assisted laser desorption/ionization time-of-flight mass spectrometry (MALDI-TOF MS) analysis (44). To evaluate the subcellular distribution of the exocyst complex in platelets, isolated platelets were resuspended in Buffer A containing protease inhibitors, sonicated on ice, and centrifuged at 300,000 × *g* for 30 min. The supernatant was regarded as cytosolic fraction and the pellet as membrane-bound fraction. SLO-permeabilized platelets were incubated at 4 °C for 15 min to allow the cytosol to leak out and centrifuged at 600 × *g* for 5 min. The supernatant was regarded as the fraction leaked out from the cells and the pellet as the fraction retained in the cells. Comparable amounts of the supernatants and the pellets were analyzed by immunoblotting with anti-RalA, anti-Sec5-N terminus, anti-Sec8, and anti-PKCα antibodies.

*Analysis of the Effect of Anti-Sec5-RBD Antibody on the Ral-Exocyst Interaction*—Glutathione-Sepharose beads coated with GST alone, GDP- or GppNHp-bound GST-RalA (amino acids 9–183) (8 μg each) were incubated with platelet cytosol (0.8 mg of proteins) in the presence of indicated concentration of anti-GST or anti-Sec5-RBD antibody at 4 °C for 1 h. After washing the beads, bead-associated proteins were analyzed by immunoblotting with anti-Sec5-N terminus polyclonal antibody and anti-Sec8 monoclonal antibody.

*Analysis of the Ral-Exocyst Interaction in Intact Platelets*—Platelets ($6 \times 10^8$ platelets/assay) isolated from freshly obtained whole blood were stimulated with 0.5 unit/ml thrombin for various periods at 30 °C. Samples were lysed (1:4, v/v) in ice-cold Buffer A containing 0.5% Triton X-100 and protease-inhibitor mixture at 4 °C for 5 min followed by centrifugation at 300,000 × *g* for 5 min. The supernatants were incubated with protein A-agarose beads (Roche Applied Science) coated with anti-Sec8-C terminus polyclonal antibody at 4 °C for 1 h. After washing the beads, bead-associated proteins were analyzed by immunoblotting with anti-RalA and anti-Sec8 monoclonal antibodies.

## RESULTS

*GppNHp, but Not GTP, Induced Dense Granule Secretion from Permeabilized Platelets*—We have previously established a semi-intact dense granule secretion assay in platelets permeabilized with SLO, using calcium chloride as a stimulus (37–41, 45). In this assay, the secretion is dependent on the exogenous addition of ATP and cytosol, and more than 50% of the serotonin stored in dense granules is released within 1 min upon stimulation with 20 μM $Ca^{2+}$.

By modification of this method, we first confirmed the previous finding that dense granules were secreted by stimulation with non-hydrolyzable GTP analogue in permeabilized platelets (7, 11). GppNHp induced the dense granule secretion in time- and concentration-dependent manners (Fig. 1, *A* and *B*) in a condition where the calculated free $Ca^{2+}$ concentration was ~20 nM (42). On the other hand, GTP did not induce the secretion of dense granules at 100 μM (data not shown) or even at 1 mM (Fig. 1*A*). Interestingly, although the addition of ATP was required for the GppNHp-induced secretion (data not shown), exogenous addition of platelet cytosol was not required, unlike for the $Ca^{2+}$-induced secretion (38). These results indicated that GppNHp and $Ca^{2+}$ stimuli utilized distinct pathways in permeabilized platelets.

*Involvement of Ral in the GppNHp-induced Dense Granule Secretion from Permeabilized Platelets*—The GppNHp dependence in the secretion suggested that some GTPases were involved in the process. Among numerous GTP-binding proteins, we focused on Ral because Ral preferentially localizes on dense granules in platelets (22) and is rapidly activated in response to agonist stimulations (17). To test whether Ral is involved in the regulation of the GppNHp-induced dense granule secretion from permeabilized platelets, we first characterized the RBD of Sec5, a Ral-binding component of the exocyst complex (24–26, 35). The interaction between Sec5-RBD and Ral is specific because it has been demonstrated that Sec5 does not bind to other small GTPases, such as RhoA, Rac1, Cdc42, Rab8, K-Ras, or H-Ras (26). We produced and purified wild-type Sec5-RBD and the Sec5-RBD T11A mutant lacking the Ral binding activity (35) as GST fusion proteins. Sec5-RBD interacted with the GppNHp-bound forms of RalA and RalB but not with GDP-bound forms (Fig. 2*A*). On the other hand, Sec5-RBD T11A did not bind either the GppNHp- or GDP-bound forms (Fig. 2*A*).

Next, we examined the state of activation of Ral in permeabilized platelets by a GTP-Ral pulldown assay using GST-Sec5-RBD. When permeabilized platelets were incubated with 100 μM GppNHp, both RalA and RalB were converted to the active forms in a time-dependent manner (Fig. 2, *B* and *C*). About 17% of total RalA or RalB were activated after a 15-min incubation with GppNHp (Fig. 2*C*). In contrast, incubation of permeabilized platelets with 1 mM GTP did not activate RalA (Fig. 2*B*). Importantly, the time course of the Ral activation was well correlated with that of the GppNHp-induced dense granule secretion (compare Figs. 1*A* and 2*C*).

We then analyzed the effects of Sec5-RBD on the GppNHp-induced secretion. The addition of Sec5-RBD in permeabilized platelets inhibited the GppNHp-induced dense granule secretion (Fig. 3*A*) in a concentration-dependent manner (Fig. 3*B*). This inhibition was presumably due to the blocking of endogenous active Ral by Sec5-RBD. On the other hand, the addition of Sec5-RBD T11A or GST did not inhibit the secretion (Fig. 3*B*). These results indicated that Ral was involved in the regulation of the GppNHp-induced dense granule secretion.